

# FAST: Topology-Aware Frequency-Domain Distribution Matching for Coreset Selection

Jin Cui<sup>\*1</sup>, Boran Zhao<sup>\*†2</sup>, Jiajun Xu<sup>2</sup>, Jiaqi Guo<sup>3</sup>, Shuo Guan<sup>2</sup>, Pengju Ren<sup>1</sup>

<sup>1</sup>State Key Laboratory of Human-Machine Hybrid Augmented Intelligence, Institute of Artificial Intelligence and Robotics, Xi’an Jiaotong University

<sup>2</sup>School of Software Engineering, State Key Laboratory of Human-Machine Hybrid Augmented Intelligence, Institute of Artificial Intelligence and Robotics, Xi’an Jiaotong University

<sup>3</sup>School of Mathematical Sciences, Nankai University

andycui@stu.xjtu.edu.cn, boranzhao@xjtu.edu.cn, mikanaffine@stu.xjtu.edu.cn  
2312195@mail.nankai.edu.cn, guanshuo@stu.xjtu.edu.cn, pengjuren@xjtu.edu.cn

## Abstract

Coreset selection compresses large datasets into compact, representative subsets, reducing the energy and computational burden of training deep neural networks. Existing methods are either: (i) DNN-based, which are inherently coupled with network-specific parameters, inevitably introducing architectural bias and compromising generalization; or (ii) DNN-free, which utilize heuristics that lack rigorous theoretical guarantees for stability and accuracy. Neither approach explicitly constrains distributional equivalence of the representative subsets, largely because continuous distribution matching is broadly considered inapplicable to discrete dataset sampling. Furthermore, prevalent distribution metrics (e.g., MSE, KL, CE, and MMD) are often incapable of accurately capturing higher-order moments differences. These deficiencies lead to suboptimal coreset performance, preventing the selected coreset from being truly equivalent to the original dataset.

We propose FAST (Frequency-domain Aligned Sampling via Topology), the first DNN-free distribution-matching coreset selection framework that formulates coreset selection task as a graph-constrained optimization problem grounded in spectral graph theory and employs the Characteristic Function Distance (CFD) to capture full distributional information (i.e., all moments and intrinsic correlations) in the frequency domain. We further discover that naive CFD suffers from a “vanishing phase gradient” issue in medium and high-frequency regions; to address this, we introduce an Attenuated Phase-Decoupled CFD. Furthermore, for better convergence, we design a

*Progressive Discrepancy-Aware Sampling strategy that progressively schedules frequency selection from low to high. This preserves global structure before refining local details, enabling accurate matching with few frequencies while preventing overfitting. Extensive experiments demonstrate that FAST significantly outperforms state-of-the-art coreset selection methods across all evaluated benchmarks, achieving an average accuracy gain of 9.12%. Compared to other baseline coreset methods, it reduces power consumption by 96.57% and achieves a 2.2× average speedup even on CPU with 1.7GB of memory, underscoring its high performance and energy efficiency.*

## 1. Introduction

Deep Neural Networks (DNNs) have achieved—and in some cases even surpassed—human-level performance across diverse domains such as vision [5, 12, 26], programming [7, 24, 31], and science [18, 28]. This remarkable success is primarily driven by the availability of massive training datasets [15, 25, 35]. However, training on such large-scale data incurs prohibitive energy costs, as illustrated in Fig. 1, the total energy consumption can reach up to  $10^3$  MWh, exceeding the annual electricity usage of numerous households by several orders of magnitude. To mitigate this challenge, a variety of dataset compression techniques have been proposed to condense large-scale datasets into compact yet representative subsets [17, 41, 45, 46]. These methods have found widespread adoption in tasks such as neural architecture search, continual learning [33, 43], and transfer learning [23].

Among existing compression techniques, coreset selection [17, 19, 29] offers superior efficiency over synthesis-based distillation [41, 45, 46] by avoiding computationally

<sup>\*</sup>Equal contribution.

<sup>†</sup>Corresponding author.

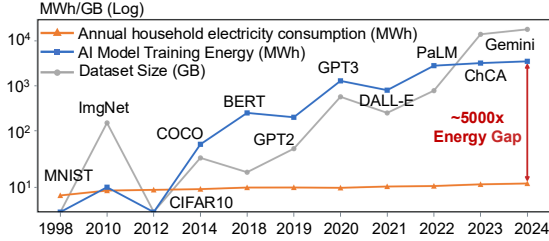


Figure 1. The energy consumption of training exceeds the annual electricity usage of numerous households by several orders of magnitude.

intensive nested gradient descent, making it ideal for on-device deployment. Furthermore, it preserves the fidelity of data and mitigates the failure modes of synthesis methods, which often struggle to generate highly discriminative samples for classification tasks with high inter-class similarity.

Existing coreset selection methods can be broadly categorized into two paradigms: (i) DNN-based approaches that adopt a proxy DNN to evaluate each sample’s contribution to training performance. While effective, these methods are intrinsically tied to specific network architectures, thereby introducing architectural bias and limiting generalization; and (ii) DNN-free methods that eschew DNNs entirely and rely on heuristic criteria, but often lack rigorous theoretical guarantees. Critically, the efficacy of coreset selection hinges on the metrics used to identify representative samples. However, neither paradigm explicitly enforces complete distributional alignment, resulting in subsets that lack comprehensive data coverage and cannot fully represent the original dataset, thereby exhibiting instability and poor generalization. Moreover, prevalent distribution metrics such as MSE [39], KL [21], MMD [16], and CE [22] are constrained by the difficulty of selecting model families or kernels [3] with appropriate representational capacity, rendering them incapable of capturing high-order moment differences or multivariate correlations [11, 34], and ultimately leading to degraded performance, as visualized in Fig. 2.

To address these issues, recent study [41] has introduced gradient-based distribution matching methods, which adopt continuous optimization in the feature space to improve matching accuracy. However, its application has been largely confined to synthesis-based dataset distillation, since direct continuous optimization in the feature space deviates from the discrete data manifold, preventing the discovery of corresponding real samples in the original dataset.

To bridge this continuous-to-discrete gap, we introduce *topology-aware* constraints based on spectral graph theory into the loss function, ensuring that the optimized samples maintain a one-to-one correspondence with the original data space and preserve critical local topological structures. This enables, for the first time, the application of distribution matching method with continuous optimization based on gradient descent to the discrete coreset selection task.

Most of important, we leverage frequency-domain features as the evaluation criterion, specifically employing the Characteristic Function Distance (CFD). The underlying Characteristic Function (CF) uniquely *captures all correlations and high-order moments* by projecting them into the frequency domain, thereby providing a more rigorous guarantee of distributional equivalence. Furthermore, we identify and address a critical *vanishing phase gradient* problem in standard CFD, where phase-magnitude coupling blinds the optimizer to medium and high-frequency details (e.g., edges and textures, as illustrated in Fig. 3). We propose a novel Attenuated Phase-Decoupled CFD (PD-CFD) to resolve this issue and experimentally validate its superiority on datasets rich in high-frequency content (e.g., DTD [10]).

We further find that the efficacy of CFD significantly depends on frequency selection. We observe that premature inclusion of high-frequency components destabilizes optimization by causing an overemphasis on fine details while mismatching the global structure. To address this, we design Progressive Discrepancy-Aware Sampling (PDAS), a curriculum-learning strategy that matches frequencies progressively from low to high, ensuring stable and accurate alignment with a minimal set of essential frequencies.

Building upon these insights, we propose Frequency-domain Aligned Sampling via Topology (FAST) framework. FAST improves accuracy by an average of 9.12% over state-of-the-art (SOTA) coreset selection methods, even when running on a CPU with only 1.7 GB of memory, while reducing power consumption by 96.57% and achieving a  $2.2\times$  speedup on average, benefited from the fast convergence realized by powerful distribution matching of our proposed methods. Our main contributions are as follows:

1. We propose a novel, topology-aware, DNN-free coreset selection framework that, for the first time, enables distribution matching in the discrete domain while eliminates architectural bias.
2. We are the first to employ Characteristic Function Distance (CFD) in coreset selection to evaluate full distributional information, and we introduce Attenuated Phase-Decoupled CFD to address the *vanishing phase gradient* issue in medium and high-frequency regions.
3. We conduct a thorough analysis of frequency selection and propose the curriculum-learning-based Progressive Discrepancy-Aware Sampling strategy for robust matching with a minimal number of frequencies.
4. Our method achieves SOTA performance with significantly lower computational overhead, making it suitable for deployment in resource-limited environments.

## 2. Related Work

**Dataset Condensation.** Dataset Condensation (DC) comprises two main branches: synthesis-based distillation [6, 41, 45, 46, 48] and sampling-based coreset selection. Core-

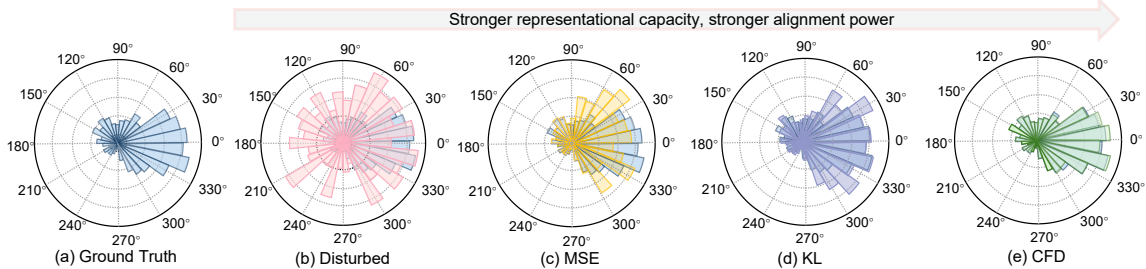


Figure 2. Comparison of distribution alignment under different metrics in frequency domain (on complex-plane). MSE aligns the mean, KL aligns both mean and variance, while CFD captures complete distributional structures in the frequency domain.



Figure 3. Low frequencies (b) capture smooth shading and coarse shapes; high frequencies (c) capture edges and fine textures. Amplitude (d) (and corresponding spectrum (e)) encodes the energy distribution across frequencies, while phase (f) specifies the spatial arrangement of structures.

set selection circumvents the prohibitive nested training overhead of distillation, offering superior efficiency, and is broadly categorized as either DNN-based or DNN-free.

DNN-based approaches typically rely on a fixed (often DNN-provided) feature embedding for geometric sampling [8, 36], or utilize training signals (e.g., losses, gradients) supplemented by adjustment mechanisms to identify informative samples [19, 20, 30, 32]. However, this deep coupling with the proxy DNN introduces strong architectural bias, leading to poor generalization and incurring significant computational overhead. DNN-free methods eliminate this bias and are more efficient, but existing work is scarce, the only representative method [47] relies on manifold reduction and heuristic grid sampling—an unreliable approach lacking stable guarantees across diverse datasets.

Critically, both paradigms face inherent limitations: (1) Their selection metrics (e.g., MSE, KL) are insufficient to capture full distributional discrepancies. (2) Their guiding principles are incomplete, either emphasizing specific training contributions, compromising generalization, or relying on heuristics that match only low-order statistics, leading to instability. As a result, the selected coresets fail to reflect the full data distribution, ultimately degrading downstream performance.

**Characteristic Function.** The Characteristic Function (CF) of a probability distribution (its Fourier transform) uniquely determines the distribution in the frequency domain, making the Characteristic Function Distance (CFD) an effective metric for comparing complex distributions. In statistics, it serves as a powerful non-parametric statistic for two-sample testing [9, 13, 14]. This capability has also been adopted in Generative Models, where CFD (or its variant, MMD [2]) is employed as a loss function to train GANs [4] by minimizing the real-to-generated discrepancy. Similarly, in domain adaptation, CFD is used as a domain discrepancy metric to learn domain-invariant representations [42]. However, to the best of our knowledge, no prior work has utilized CFD as an evaluation metric for coreset selection.

The only work applying frequency-domain features to dataset compression is NCFM [41], but it is limited to synthesis-based methods and thus inapplicable to discrete coreset selection. Furthermore, NCFM suffers from two critical limitations: (1) It relies on DNNs for feature extraction and frequency selection, thereby inheriting architectural bias, lacking interpretability, and leading to sub-optimal frequency selection. (2) Its loss function couples phase with magnitude, failing to distinguish phase differences in high-frequency regions where magnitude decays.

## 3. Method

### 3.1. Graph Construction

To provide a stable optimization space for distribution matching, we first capture the intrinsic manifold structure of the data. We construct a multi-scale weighted undirected graph  $\mathbf{B} \in \mathbb{R}^{N \times N}$  based on the fuzzy topological theory from UMAP [27], which serves as the foundation for all subsequent feature extraction and topological constraints.

**Multi-Scale Manifold Graph Construction.** To capture geometry at multiple scales, rather than relying on a single  $k$ -nearest neighbor scale, we construct graphs for a set of  $k$ -nearest neighbor scales  $\{k_1, k_2, \dots\}$ . For each scale  $k$  and data point  $x_i$ , we find the local connectivity distance  $\rho_i$  and

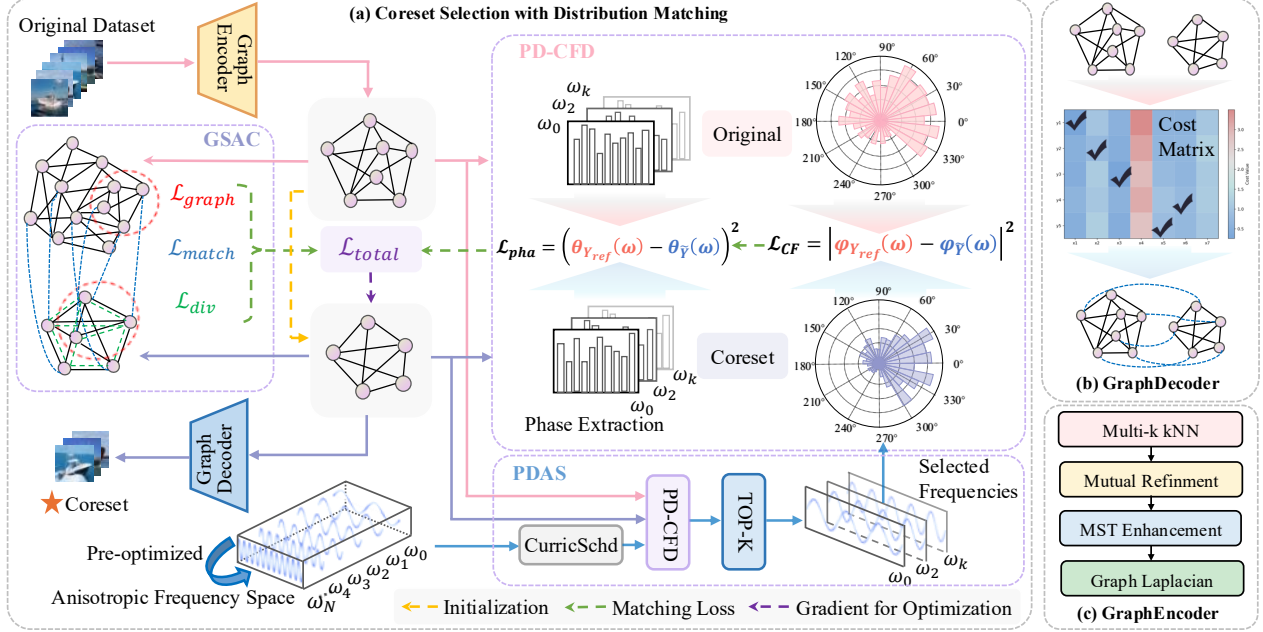


Figure 4. (a) Overview of proposed FAST. Graph-Structure-Aware Constraints (GSAC) preserves topological consistency, while Progressive Discrepancy-Aware Sampling (PDAS) progressively aligns distributions via phase-decoupled characteristic function distance (PD-CFD). (b) Graph Decoder. Maps the optimized coreset back to the original data space, ensuring structural consistency. (c) Graph Encoder. Constructs the graph topology based-on spectral graph theory.

the local scale factor  $\sigma_i$  by solving the following equation:

$$\sum_{j=1}^k \exp\left(\frac{-\max(0, d(\mathbf{x}_i, \mathbf{x}_{i_j}) - \rho_i)}{\sigma_i}\right) = \log_2(k) \quad (1)$$

This defines the directed edge weights. We first symmetrize these weights for each scale  $k$  using the probabilistic t-conorm (a fuzzy set union),  $\mathbf{A}_k = \mathbf{A}_k + \mathbf{A}_k^T - \mathbf{A}_k \circ \mathbf{A}_k^T$ . Subsequently, we fuse the graphs  $\mathbf{A}_k$  from all scales into a single multi-scale adjacency matrix  $\mathbf{B}$  by iteratively applying the same fuzzy set union. Finally, we ensure global connectivity by incorporating the graph’s Minimum Spanning Tree (MST) via  $\mathbf{B} = \mathbf{B} \cup \text{MST}(\mathbf{B})$ .

**Spectral Embedding as Manifold Features.** From the multi-scale graph  $\mathbf{B}$ , we compute its Symmetric Normalized Laplacian:

$$\mathcal{L}_{\text{sym}} = \mathbf{I} - \mathbf{D}^{-1/2} \mathbf{B} \mathbf{D}^{-1/2} \quad (2)$$

where  $\mathbf{D}$  is the diagonal degree matrix. The eigenvectors of  $\mathcal{L}_{\text{sym}}$  serve as a discrete approximation of the manifold’s Laplace-Beltrami operator, revealing its intrinsic geometry. We extract the  $d$  eigenvectors ( $d \ll N$ ) corresponding to the smallest non-zero eigenvalues to form the  $N \times d$  manifold feature matrix  $\mathbf{V}_{\text{full}}$ . This matrix provides a robust representation of the original data’s geometry and serves as the reference for all subsequent optimizations.

### 3.2. Topology-Aware Alignment and Regularization

Our method optimizes a continuous coreset representation  $\tilde{Y} \in \mathbb{R}^{M \times d}$  ( $M \ll N$ ) by aligning its frequency-domain

features with the reference  $\mathbf{V}_{\text{full}}$ . The core challenge lies in the continuous-to-discrete gap:  $\tilde{Y}$  must ultimately map back to  $M$  discrete samples from  $\mathbf{V}_{\text{full}}$ . To address this, the optimization is guided by a composite constraint system that enforces both diversity and topological alignment.

**Diversity Constraint.** To ensure  $\tilde{Y}$  spans the feature space and covers the full distribution, we introduce a diversity loss  $\mathcal{L}_{\text{div}}$  based on Determinantal Point Processes (DPP). We minimize  $\mathcal{L}_{\text{div}} = -\log \det(\mathbf{K})$ , where  $\mathbf{K} = \Psi \Psi^T + \delta \mathbf{I}$  is the Gram matrix of the RFF features ( $\Psi$ ) of  $\tilde{Y}$ , explicitly penalizing feature redundancy.

**Graph-Aware Alignment Constraint.** To bridge the gap between continuous optimization and discrete selection, we introduce a complementary constraint inspired by graph alignment (GUNN), which maintain structural consistency between  $\tilde{Y}$  and a subset of  $\mathbf{V}_{\text{full}}$  throughout the optimization. This constraint is composed of two main components.

At each optimization step, we find an optimal, bijective mapping  $\pi : \{1, \dots, M\} \rightarrow \{1, \dots, N\}$  by solving the linear assignment problem using the Hungarian Algorithm. This mapping assigns each point  $\mathbf{y}_i \in \tilde{Y}$  to a unique real feature  $\mathbf{v}_j \in \mathbf{V}_{\text{full}}$ . The assignment is guided by a graph-aware cost matrix  $\mathbf{C} \in \mathbb{R}^{M \times N}$  whose entries consider both Euclidean proximity and topological significance:

$$C_{i,j} = \frac{\|\mathbf{y}_i - \mathbf{v}_j\|^2}{\deg(\mathbf{v}_j) + \epsilon} \quad (3)$$

where  $\deg(\mathbf{v}_j)$  is the degree of node  $\mathbf{v}_j$  in the original graph  $\mathbf{B}$ , anchoring points in continuous space to real nodes that

are central to the manifold’s topology.

Based on the computed optimal mapping  $\pi$ , we apply two alignment losses: (i) A *Positional Loss* ( $\mathcal{L}_{\text{match}}$ ) that pulls each  $\mathbf{y}_i$  to its assigned discrete anchor  $\mathbf{V}_{\text{full}}[\pi(i)]$ :

$$\mathcal{L}_{\text{match}} = \frac{1}{M} \sum_{i=1}^M \|\mathbf{y}_i - \mathbf{V}_{\text{full}}[\pi(i)]\|^2 \quad (4)$$

and (ii) A *Topological Loss* ( $\mathcal{L}_{\text{graph}}$ ) that preserves the original structure of the selected anchors. Let  $\mathcal{L}_{\text{sub}}$  be the  $M \times M$  submatrix of  $\mathcal{L}_{\text{sym}}$  indexed by  $\pi$ . The loss is the Laplacian regularizer:

$$\mathcal{L}_{\text{graph}} = \text{Tr}(\tilde{Y}^T \mathcal{L}_{\text{sub}} \tilde{Y}) \quad (5)$$

$\mathcal{L}_{\text{graph}}$  ensures that if anchor points  $\mathbf{v}_{\pi(i)}, \mathbf{v}_{\pi(j)}$  are strongly connected in the original manifold, their continuous counterparts  $\mathbf{y}_i, \mathbf{y}_j$  also remain close in the optimization space.

### 3.3. Phase-Decoupled Characteristic Function Distance

We optimize the coreset  $\tilde{Y}$  by minimizing its distance in the CF space from the reference dataset  $Y_{\text{ref}}$ . We build our objective function by first defining the standard CFD.

**From CF to CFD.** The theoretical Characteristic Function (CF) of a  $d$ -dimensional distribution  $P$  provides a complete frequency-domain representation, defined as  $\varphi_P(t) = \mathbb{E}_{X \sim P}[e^{i\langle t, X \rangle}] = \int_{\mathbb{R}^d} e^{i\langle t, x \rangle} dP(x)$ , where  $t \in \mathbb{R}^d$  is the frequency vector. In practice, we use the Empirical Characteristic Function (ECF) computed from a set of samples  $\mathcal{Y}$ :

$$\varphi_{\mathcal{Y}}(t) = \frac{1}{|\mathcal{Y}|} \sum_{y \in \mathcal{Y}} e^{i\langle t, y \rangle} \quad (6)$$

Our goal is to match the ECF  $\varphi_{\tilde{Y}}(t)$  of the coreset, to that of the reference set  $\varphi_{Y_{\text{ref}}}(t)$ , over a frequency distribution  $t$ .

The  $L^2$  CFD measures the distance between two theoretical distributions  $P$  and  $Q$  by integrating the squared difference of their CFs over a weighting function  $w(t)$ :  $D^2(P, Q) = \int_{\mathbb{R}^d} |\varphi_P(t) - \varphi_Q(t)|^2 w(t) dt$ . In practice, the empirical CFD (ECFD) replaces theoretical CFs with their empirical estimates and approximates the integral as an expectation over a frequency sampling distribution  $p(t)$  (corresponding to  $w(t)$ ):

$$\mathcal{L}_{\text{CFD}} = \mathbb{E}_{t \sim p(t)} [|\varphi_{\tilde{Y}}(t) - \varphi_{Y_{\text{ref}}}(t)|^2] \quad (7)$$

This standard ECFD serves as the foundation for our main loss  $\mathcal{L}_{\text{main}}$ .

**The Vanishing Phase Gradient Problem.** To analyze the behavior of  $\mathcal{D}_w^2$ , we examine its integrand in polar form with magnitude  $A(t) = |\varphi(t)|$  and phase  $\theta_{\varphi}(t)$  (omitting  $t$  for brevity):

$$|\varphi_{\tilde{Y}} - \varphi_{Y_{\text{ref}}}|^2 = A_{\tilde{Y}}^2 + A_{Y_{\text{ref}}}^2 - 2A_{\tilde{Y}}A_{Y_{\text{ref}}}\cos(\theta_{\tilde{Y}} - \theta_{Y_{\text{ref}}}) \quad (8)$$

This expansion exposes the *Vanishing Phase Gradient* problem: the contribution of the phase difference  $\Delta\theta = (\theta_{\tilde{Y}} - \theta_{Y_{\text{ref}}})$  is scaled by (coupled with) the magnitude product  $A_{\tilde{Y}}A_{Y_{\text{ref}}}$ . According to the Riemann–Lebesgue lemma

(see Appendix), magnitudes  $A(t) \rightarrow 0$  as frequency  $\|t\| \rightarrow \infty$ . This coupling suppresses the phase gradient in medium-high frequency regions, causing naive CFD to ignore essential information before the phase degenerates into high-frequency noise.

**Phase-Decoupled CFD Loss.** To address this, we introduce a Phase-Decoupled loss function  $\mathcal{L}_{\text{CF}}$ . This loss is defined for each sampled frequency  $\omega \sim p(t)$  used in the Monte Carlo estimation:

$$\mathcal{L}_{\text{CF}}(\omega) = |\varphi_{Y_{\text{ref}}}(\omega) - \varphi_{\tilde{Y}}(\omega)|^2 + \lambda_{\phi}(\omega)(\theta_{Y_{\text{ref}}}(\omega) - \theta_{\tilde{Y}}(\omega))^2 \quad (9)$$

where  $\theta(\omega)$  denotes the phase angle, and  $\lambda_{\phi}(\omega)$  represents a phase-penalty term. Constant penalty  $\lambda_{\phi}$  is suboptimal as it amplifies high-frequency noise (where  $A(t) \rightarrow 0$  and phase  $\theta(t)$  is unstable). Therefore, we propose PD-CFD, using a penalty  $\lambda_{\phi}(\omega)$  that adaptively decays in noisy, high-frequency regions:

$$\lambda_{\phi}(\omega) = \frac{\lambda_p}{1 + \alpha\|\omega\|^2} \quad (10)$$

Here,  $\lambda_p$  and  $\alpha$  control the penalty and its decay rate. This formulation amplifies the mid-range phase signal (where  $A(\omega)$  has decayed but  $\lambda_{\phi}(\omega)$  remains significant) while suppressing noise. The final objective is the average of this loss over  $k$  adaptively sampled frequencies  $\{\omega_j\}_{j=1}^k$ :

$$\mathcal{L}_{\text{main}} = \frac{1}{k} \sum_{j=1}^k \mathcal{L}_{\text{CF}}(\omega_j) \quad (11)$$

### 3.4. Progressive Discrepancy-Aware Sampling

**Moment Encoding in Characteristic Functions.** The characteristic function  $\varphi(t)$  provides a complete representation of a distribution by systematically encoding all of its moments. The mixed partial derivatives of  $\varphi(t)$  evaluated at  $t = 0$  correspond directly to the mixed raw moments,  $\partial^{\alpha}\varphi(0) = i^{|\alpha|}\mathbb{E}[X^{\alpha}]$ . This property enables  $\varphi(t)$  to be expressed through its multivariate Taylor expansion:

$$\varphi(t) = \sum_{|\alpha| \leq m} \frac{1}{\alpha!} \partial^{\alpha}\varphi(0)t^{\alpha} = \sum_{|\alpha| \leq m} \frac{i^{|\alpha|}}{\alpha!} \mathbb{E}[X^{\alpha}]t^{\alpha} \quad (12)$$

This expansion reveals that the value of  $\varphi(t)$  at any nonzero frequency  $t$  is a weighted polynomial combination of all its constituent moments  $\mathbb{E}[X^{\alpha}]$ . Furthermore, the log-CF,  $\psi(t) = \log \varphi(t)$ , similarly encodes the mixed cumulants  $\kappa_{\alpha}$ , which capture higher-order dependencies, via its derivatives at the origin:  $\partial^{\alpha}\psi(0) = i^{|\alpha|}\kappa_{\alpha}$ . Detailed derivations are provided in the Appendix.

The objective of the CFD is to estimate the integral measure  $\mathcal{D}_w^2(P, Q) = \int |\varphi_P(t) - \varphi_Q(t)|^2 w(t) dt$ . The moment-encoding property implies that if two distributions  $P$  and  $Q$  differ in any  $k$ -th order moment, their characteristic functions  $\varphi_P(t)$  and  $\varphi_Q(t)$  must diverge in certain regions of the frequency domain. Therefore, the frequency sampling

distribution  $p(t)$  (corresponding to  $w(t)$ ) is a critical hyperparameter that determines the estimator’s sensitivity to specific types of distributional discrepancies.

**Anisotropic Frequency Initialization.** Instead of adopting a standard Gaussian frequency bank  $\mathcal{N}(0, I)$ , we first perform an initialization stage to construct an anisotropic frequency space that is sensitive to the current data distribution  $Y_{\text{ref}}$ . This stage partitions the frequency selection range into low, medium, and high-frequency bands based on the norm  $\|\omega\|$ . For each band, we optimize a set of anisotropic scaling (variance) coefficients  $\mathbf{s}_{\text{band}}$  by maximizing the CF difference within that band:

$$\mathbf{s}_{\text{band}}^* = \arg \max_{\mathbf{s}} \mathbb{E}_{t \sim \mathcal{N}(0, \text{diag}(\mathbf{s}^2))} [\mathcal{L}_{CF}(t) \mid t \in \text{Band}] \quad (13)$$

This procedure assigns a data-driven anisotropic scaling to each frequency in the frequency space, enhancing sensitivity to the structural differences of the dataset. The resulting *Anisotropic Frequency Library (AFL)* serves as the foundation for subsequent progressive sampling.

**Progressive Discrepancy-Aware Sampling.** In the main optimization loop, we employ a curriculum-based strategy for adaptive frequency selection from the pre-optimized AFL. We define a frequency norm upper bound  $\tau_t$  that progressively increases with iteration  $t$ . The candidate frequency pool at iteration  $t$  is restricted to  $C_t = \{\omega \in \text{AFL} \mid \|\omega\| \leq \tau_t\}$ . This progressive strategy ensures the model first matches low-frequency global statistics before gradually shifting to high-frequency fine-grained structures. Within  $C_t$ , importance sampling is performed based on the current discrepancy. The probability  $p_t(\omega)$  of sampling a frequency  $\omega \in C_t$  is proportional to a composite score:

$$p_t(\omega) \propto \mathcal{L}_{CF}(\omega) \cdot \mathcal{D}(\omega) \quad (\omega \in C_t) \quad (14)$$

where  $\mathcal{L}_{CF}(\omega)$  is the total phase-decoupled loss defined in Eq. (9),  $\mathcal{D}(\omega)$  represents a diversity term that penalizes high correlations with previously selected frequencies. This sampling strategy ensures that each batch  $\mathcal{B}_t$  for gradient estimation consistently focuses on the most informative, high-discrepancy frequencies within the current boundary  $\tau_t$ .

### 3.5. Joint Optimization

We guide the gradient descent optimization of the coreset  $\tilde{Y}$  by minimizing a comprehensive loss function  $\mathcal{L}_{\text{total}}$  that combines the primary frequency-domain matching loss with topological regularization terms:

$$\mathcal{L}_{\text{total}} = \mathcal{L}_{\text{main}} + \lambda_{\text{div}} \mathcal{L}_{\text{div}} + \mathcal{L}_{\text{align}} \quad (15)$$

where  $\mathcal{L}_{\text{align}}$  is a composite constraint term that includes two key sub-terms from our dual alignment constraint:

$$\mathcal{L}_{\text{align}} = \lambda_{\text{match}} \mathcal{L}_{\text{match}} + \lambda_{\text{graph}} \mathcal{L}_{\text{graph}} \quad (16)$$

## 4. Experiment

### 4.1. Setup

**Datasets.** We evaluate FAST on multiple benchmarks of varying scales and complexities: (1) *Small-scale*: CIFAR-

10 (10 classes, 60k  $32 \times 32$  images), CIFAR-100 (100 classes, 60k  $32 \times 32$  images), and SVHN (10 classes, 99k  $32 \times 32$  images). (2) *Medium-scale*: Tiny ImageNet (200 classes, 120k  $64 \times 64$  images). (3) *Large-scale and texture-rich*: DTD (47 classes, 5,640 images resized to  $224 \times 224$ ) and RESISC45 (45 classes, 31k  $256 \times 256$  images).

**Models.** We comprehensively evaluate the generalization of our method on a diverse range of network architectures. These include standard CNNs (ResNet18, ResNet50) as general benchmarks, lightweight CNNs (ShuffleNetV2, MobileNetV2) and a Transformer (ViT). All models are trained for 200 epochs using SGD with a momentum of 0.9, weight decay of  $5 \times 10^{-4}$ . The batch size is set to 256 for  $32 \times 32$  datasets and 64 for  $224 \times 224$  or  $256 \times 256$  datasets. Sampling ratios of 10%, 20%, and 30% are used to assess performance under different compression levels.

**Baseline methods.** We compare FAST against a comprehensive set of coreset selection baselines, categorized as shown in Table 1. Among them, only FAST and NMS are DNN-free methods.

**Hardware Platform.** Experiments are conducted on two platforms: (1) *CPU/GPU*: Intel(R) Xeon(R) Platinum 8358P CPU, NVIDIA A100 GPU (80 GB), and 512 GB system memory; (2) *Edge*: Rockchip RK3588 ( $4 \times$  Cortex-A76 and  $4 \times$  Cortex-A55, NPU disabled) with 4 GB memory. Energy measurements are obtained using Zeus toolkit [44] and Intel’s Running Average Power Limit (RAPL) interface.

## 4.2. Results and Analysis

**Overall Performance.** We validated FAST’s effectiveness across datasets of different scales and keep rates. As demonstrated in Table 1, FAST consistently outperforms all competing baselines. It achieves an average accuracy improvement of 17.63% over DNN-based methods and 9.12% over SOTA DNN-free methods. Critically, FAST demonstrates a substantial 21.93% average performance gain on DTD and RESISC45, datasets characterized by complex textures and edges (further analyzed in Appendix).

This SOTA performance derives from optimizing full distributional equivalence rather than model-dependent information and heuristics (e.g., *learning difficulty* or *training trajectory*). As shown in Fig. 5, we observe a positive correlation between the coreset’s distributional alignment and downstream accuracy, demonstrating the robustness of this model-agnostic approach. The exceptional performance on complex datasets directly stems from the performance of PD-CFD to capture the higher-order moments and fine-grained structures (textures, edges) that other metrics miss while also resolving the *vanishing phase gradient* problem.

**Cross-Architecture Generalization.** As demonstrated in Fig. 6, FAST exhibits strong cross-architecture generalization. When evaluated across diverse architectures at multiple keep rates 10%, 20%, 30%, our coreset shows a negli-

Table 1. Results of FAST on CIFAR-10/100, SVHN, TinyImageNet, and high resolution datasets DTD and RESISC-45. (Dist. M.: Distribution Matching, Grid S.: Grid Sampling, Des. B.: Decision Boundary, Grad. M.: Gradient Matching, Bil. O.: Bilevel Optimization)

| Category      | Dataset Ratio(%) | CIFAR-10     |              |              | CIFAR-100    |              |              | RESISC-45    |              |              | SVHN         |              |              | DTD          |              |              | TinyImageNet |              |              |
|---------------|------------------|--------------|--------------|--------------|--------------|--------------|--------------|--------------|--------------|--------------|--------------|--------------|--------------|--------------|--------------|--------------|--------------|--------------|--------------|
|               |                  | 10           | 20           | 30           | 10           | 20           | 30           | 10           | 20           | 30           | 10           | 20           | 30           | 10           | 20           | 30           | 10           | 20           | 30           |
| Dist. M.      | FAST             | <b>90.32</b> | <b>93.39</b> | <b>94.93</b> | <b>66.61</b> | <b>72.79</b> | <b>75.85</b> | <b>85.00</b> | <b>89.32</b> | <b>91.14</b> | <b>92.86</b> | <b>94.53</b> | <b>95.30</b> | <b>45.77</b> | <b>54.69</b> | <b>61.85</b> | <b>34.55</b> | <b>51.49</b> | <b>56.85</b> |
| Grid S.       | NMS              | 86.57        | 90.18        | 92.58        | 55.13        | 63.77        | 68.79        | 74.26        | 80.12        | 83.37        | 91.76        | 93.89        | 94.08        | 38.63        | 50.28        | 59.94        | 31.41        | 47.97        | 52.30        |
| Geometry      | Herding          | 71.49        | 72.87        | 78.37        | 40.44        | 50.19        | 54.89        | 36.57        | 49.62        | 56.86        | 61.72        | 86.50        | 93.00        | 17.02        | 26.84        | 45.22        | 22.24        | 39.55        | 49.78        |
|               | kCenter          | 77.82        | 83.99        | 88.63        | 41.29        | 53.58        | 61.33        | 69.45        | 80.36        | 83.54        | 81.73        | 90.33        | 93.36        | 26.22        | 37.64        | 44.46        | 22.06        | 42.01        | 52.48        |
| Scoring       | Entropy          | 56.37        | 68.92        | 81.68        | 25.93        | 39.49        | 49.54        | 47.18        | 65.62        | 76.38        | 69.67        | 90.19        | 94.05        | 17.25        | 29.58        | 33.82        | 14.61        | 28.12        | 41.45        |
|               | Forget           | 69.07        | 80.63        | 87.18        | 48.07        | 58.32        | 65.70        | 72.64        | 79.98        | 81.42        | 77.50        | 91.81        | 93.90        | 36.73        | 50.24        | 55.33        | 30.31        | 47.84        | 53.86        |
|               | GraNd            | 45.46        | 62.67        | 75.48        | 19.64        | 27.89        | 39.85        | 35.72        | 55.70        | 69.25        | 50.99        | 86.47        | 92.85        | 24.60        | 37.28        | 41.33        | 10.45        | 20.07        | 30.09        |
| Des. B.       | Cal              | 81.76        | 81.88        | 85.86        | 56.04        | 63.23        | 68.12        | 64.22        | 70.36        | 73.15        | 81.19        | 87.69        | 90.19        | 40.45        | 49.72        | 58.07        | 30.92        | 47.41        | 52.86        |
|               | Dfool            | 59.78        | 75.19        | 81.21        | 33.47        | 43.82        | 53.20        | 57.79        | 70.16        | 76.71        | 67.33        | 87.88        | 93.07        | 24.88        | 40.10        | 48.79        | 21.74        | 40.71        | 47.85        |
| Grad. M.      | Craig            | 61.21        | 70.01        | 81.24        | 36.45        | 43.17        | 53.05        | 61.23        | 74.21        | 77.02        | 65.75        | 89.63        | 93.15        | 37.18        | 46.57        | 50.90        | 24.71        | 38.05        | 45.14        |
|               | GradM            | 60.73        | 68.46        | 78.85        | 32.47        | 43.47        | 48.31        | 52.62        | 62.94        | 73.32        | 62.17        | 86.24        | 92.62        | 33.49        | 46.41        | 53.44        | 27.35        | 39.60        | 50.25        |
| Bil. O.       | Glister          | 57.42        | 69.45        | 79.22        | 31.24        | 40.83        | 50.52        | 53.01        | 62.84        | 72.12        | 58.70        | 86.23        | 92.36        | 34.15        | 45.81        | 49.90        | 26.07        | 39.09        | 49.50        |
| Submod.       | FL               | 78.83        | 82.55        | 86.25        | 53.62        | 58.38        | 62.99        | 76.05        | 81.27        | 83.14        | 80.92        | 90.08        | 93.22        | 40.60        | 45.46        | 44.70        | 31.75        | 45.04        | 50.99        |
|               | GC               | 85.02        | 85.34        | 89.06        | 58.18        | 64.86        | 69.22        | 70.57        | 75.91        | 78.04        | 88.24        | 90.96        | 93.13        | 35.62        | 50.45        | 54.71        | 31.66        | 46.76        | 51.88        |
|               | DQ               | 85.21        | 87.90        | 90.98        | 55.61        | 60.12        | 64.67        | 72.12        | 78.37        | 80.12        | 90.07        | 92.24        | 93.18        | 36.12        | 49.13        | 55.84        | 31.24        | 45.79        | 52.03        |
| Whole Dataset |                  | 95.56        |              |              | 80.59        |              |              | 94.01        |              |              | 96.37        |              |              | 71.65        |              |              | 66.35        |              |              |

Table 2. Comparison of computational efficiency. (FAST is CPU-only, incurring zero GPU overhead)

| Works     | FAST-CPU     | FAST-EDGE   | kCenter | NMS   | DQ    | Cal   | Craig | DeepFool | GraNd  | Forgetting | GradM | Glister | Submodular | Uncertainty |
|-----------|--------------|-------------|---------|-------|-------|-------|-------|----------|--------|------------|-------|---------|------------|-------------|
| Time/s    | <b>353.0</b> | 960.0       | 616.7   | 398.0 | 426.3 | 542.8 | 437.9 | 1079.0   | 4403.0 | 410.3      | 431.4 | 425.0   | 811.3      | 414.3       |
| Energy/Wh | 1.409        | <b>0.67</b> | 50.66   | 21.01 | 34.57 | 42.35 | 37.2  | 96.46    | 402.4  | 33.81      | 35.47 | 39.36   | 59.02      | 39.05       |
| Accuracy  | <b>90.32</b> | 90.31       | 78.2    | 88.0  | 85.2  | 72.8  | 64.6  | 63.3     | 54.6   | 68.5       | 63.9  | 69.8    | 76.0       | 60.7        |

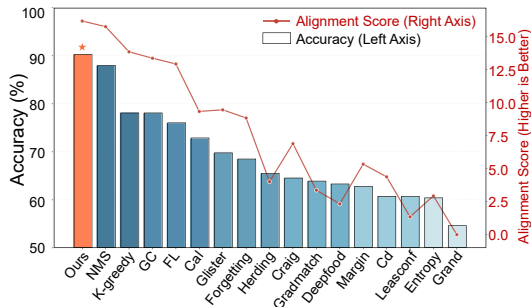


Figure 5. Relationship between downstream training accuracy and distributional equivalence. Results indicate that enforcing distributional equivalence leads to improved performance.

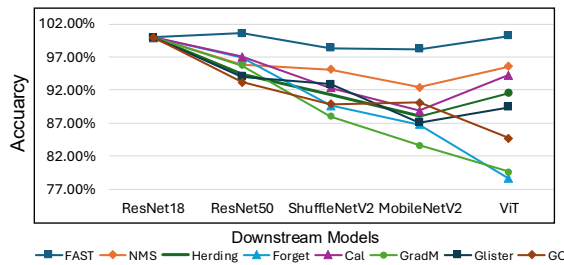


Figure 6. Cross-model generalization (Normalized). DNN-based methods suffer from performance degradation when transferring to other architectures while DNN-free approaches (FAST and NMS) remain stable performance.

ble accuracy drop (average 0.53%, even even achieves accuracy gains on some models) upon cross-architecture transfer, while competing DNN-free and DNN-based methods degrade by 3.02% and 8.68% on average.

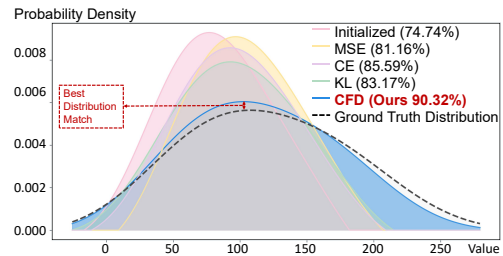


Figure 7. Ablation on distribution alignment with different metrics

This strong generalization confirms that FAST is a truly DNN-free method which seeks fundamental distributional equivalence rather than fitting a proxy model. By avoiding architectural bias, the resulting coreset faithfully mimics the full dataset’s behavior across diverse downstream scenarios, embodying a valuable *Write once, run anywhere* property.

**Computational Efficiency.** Given the importance of computational efficiency, especially on resource-constrained edge devices, we evaluate FAST’s efficiency on CIFAR-10 (10% keep rate) against strong baselines. As detailed in Table 2, we assess the total cost (sampling and training with early stopping) via runtime and energy. As shown, DNN-based methods, that require network inference for sampling, inevitably suffer from high energy consumption and slow sampling speeds. While gradient or trajectory-based methods may converge faster during training, their substantial sampling overhead negates this benefit. In contrast, FAST not only drastically reduces sampling time but also enables downstream models to achieve comparable accuracy with fewer training epochs. Furthermore, the *FAST-edge* results

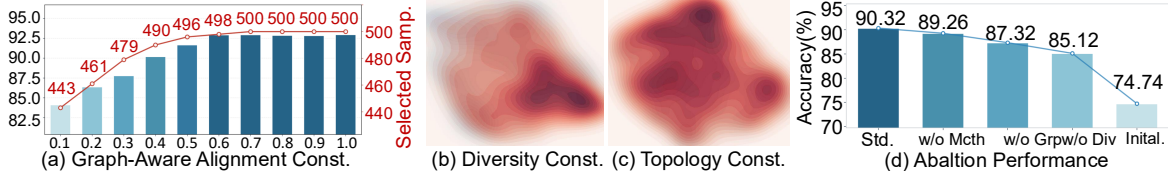


Figure 8. Ablation on graph regulations. Removing any of the three constraints—(a) GUNN ( $\mathcal{L}_{align}$ ), (b) DPP ( $\mathcal{L}_{div}$ ), or (c) graph regularization ( $\mathcal{L}_{graph}$ )—leads to degraded alignment, coverage, or topology, confirming their complementary roles in maintaining stability.

in Table 2, confirming its potential to be deployed on edge devices with limited resources.

**Performance on LLM Datasets.** We evaluate FAST on LLM tuning using the Alpaca [37] dataset. Coresets with 10%, 20% and 30% keep ratios are sampled to finetune LLaMA-7B [38] and the resulting models were assessed on the InstructEval benchmark [1]. FAST surpasses the SOTA DNN-free method by 2.6% in average accuracy, demonstrating its effectiveness on semantically rich LLM tasks. Detailed results and discussion are provided in Appendix.

### 4.3. Ablation

**Ablation on Distribution Metrics.** Building on our analysis in Fig. 2, we ablate the distribution metric on CIFAR-10 (10% keep rate, ResNet18 backbone) by replacing PD-CFD with KL, CE, and MSE, holding all other parameters constant. As shown in Fig. 7, using MSE as the metric results in significant high-order moment deviations and a 9.16% accuracy drop. Similarly, KL and CE, while improving variance alignment, still fail to match skewness and kurtosis, causing accuracy drops of 7.15% and 4.73%, respectively.

Since the effectiveness of the MMD method directly depends on the chosen kernel function, we will not expand the discussion here. But when the chosen kernel is insufficient to align high-order moments, the MMD method still cannot guarantee complete distribution alignment. We provide more detailed proof in Appendix.

**Ablation on Spectral Graph Regularization.** We conduct an ablation study to quantify the efficacy of our graph constraints. Results in Fig. 8 demonstrate the necessity of each component. Lacking GUNN ( $\mathcal{L}_{align}$ ), optimized points *clump* and map to a few identical samples, causing degradation in sampling quality. Without DPP ( $\mathcal{L}_{div}$ ), points are attracted to a few high-density modes, resulting in poor coverage. Removing graph regularization ( $\mathcal{L}_{graph}$ ) disrupts local topology by inducing excessive local clustering.

These failures highlight the core difficulty of addressing a discrete sampling task through continuous optimization. The continuous-to-discrete gap causes gradient descent (with only  $\mathcal{L}_{CF}$ ) to converge to degenerate solutions where multiple proxies  $\tilde{y}_i$  collapse into a single mode, shrinking the effective coreset. Our constraints bridge this gap: DPP ( $\mathcal{L}_{div}$ ) enforces spatial diversity in the continuous space, while GUNN ( $\mathcal{L}_{align}$ ) and  $\mathcal{L}_{graph}$  ensures topological consistency with the discrete manifold, preventing mode collapse and ensuring a stable, representative coreset.

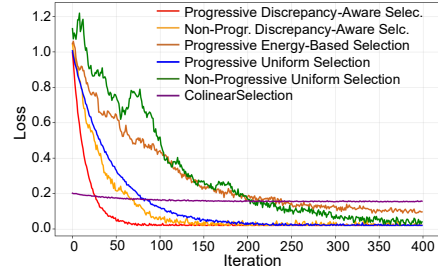


Figure 9. Ablation on PDAS. PDAS achieves stable and rapid convergence by progressively selecting discriminative frequencies, while other strategies yield unstable and suboptimal optimization.

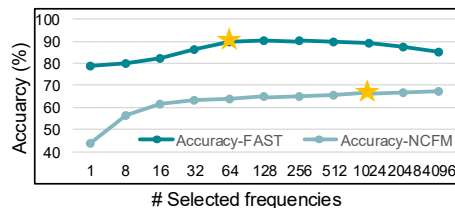


Figure 10. Effect of the number of selected frequencies.

**Ablation on Frequency Selection.** We validate our PDAS by fixing the frequency count (64) and comparing it against baselines in Fig. 9. The results confirm the critical importance of the selection strategy: (1) A worst-case collinear set degenerates the effectiveness of the CFD metric, causing optimization failure. (2) Magnitude-based Top-K selection performs poorly, as it ignores the distributional discrepancies and fails to select the most discriminative frequencies. (3) Non-progressive strategies are also suboptimal, as their erratic global selection (e.g., alternating between low and high frequencies) leads to unstable convergence. In contrast, our adaptive, curriculum-based PDAS achieves optimal matching, stably converges within fewer iterations.

We further analyze the impact of the total frequency count, as illustrated in Fig. 10. FAST saturates significantly faster and requires far fewer frequencies to reach optimal performance than the NCFM baseline. This high frequency utilization efficiency is attributable to PDAS prioritizing frequencies with the largest contribution to the current distributional discrepancy under pre-optimized anisotropic frequency distribution. This not only yields superior performance but also reduces the computational overhead of CFD.

**Ablation on Phase Constraint.** We evaluate the phase-decoupled constraint ( $\lambda_p$ ) on the detail-rich RESISC45 dataset ( $\alpha$  fixed at 1.2). As shown in Fig. 11, performance

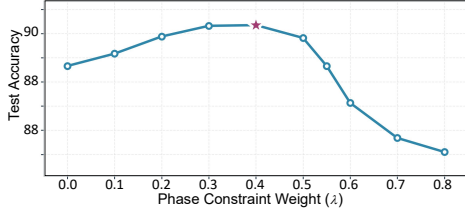


Figure 11. Ablation on phase-decoupled constraint. Performance peaks at  $\lambda_p = 0.4$ , while larger weights introduce noise and degrade alignment.

peaks at  $\lambda_p = 0.3$ , confirming its effectiveness in reinforcing high-frequency structures. For  $\lambda_p > 0.4$ , overemphasis on phase leads to high-frequency noise and degraded global consistency, reducing overall distributional alignment. To verify its generality, we integrate the optimal  $\lambda_p = 0.3$  into NCFM [41], achieving a 19.12% accuracy gain on the detail-rich CUB-200-2011 [40] dataset at IPC=10, demonstrating its robust ability to capture fine-grained structures. Detailed results are provided in the Appendix.

## 5. Conclusion

In this work, we introduced FAST, the first DNN-free distribution-matching coreset selection framework that formulates coreset selection task as a graph-constrained optimization problem grounded in spectral graph theory and employs the Characteristic Function Distance (CFD) to capture full distributional information (i.e., all moments and intrinsic correlations) in the frequency domain. Our phase-decoupled CFD formulation further resolves the amplitude-phase coupling that obscures medium and high-frequency structural information, enabling accurate preservation of fine-grained semantics and high-order dependencies.

Extensive experiments across image classification, fine-grained recognition, texture and remote-sensing datasets, and LLM instruction tuning demonstrate that FAST consistently outperforms both DNN-based and DNN-free baselines. Moreover, FAST’s excellent performance on LLM datasets further suggests that high-level semantic structure can be retained through spectral-graph-based distribution alignment, without explicit reliance on neural feature extractors. By leveraging geometric and frequency-domain signals, FAST preserves the underlying semantic neighborhood relations required for downstream reasoning. These experiments jointly demonstrate the robustness and broad generalization ability of FAST, even on tasks that rely heavily on semantic consistency.

Beyond accuracy, FAST also delivers significant efficiency gains. Since FAST operates completely without neural network inference, and our PDAS strategy prioritizes only the most discriminative frequencies, the computation required for distribution alignment is drastically reduced. Furthermore, our graph-based manifold construc-

tion avoids the repeated forward passes central to traditional gradient- or loss-based methods, which significantly lowers the sampling cost and highlights FAST’s practical utility for resource-constrained environments.

## References

- [1] Anirudh Ajith, Chris Pan, Mengzhou Xia, Ameet Deshpande, and Karthik Narasimhan. Instructeval: Systematic evaluation of instruction selection methods. In *Findings of the Association for Computational Linguistics: NAACL 2024, Mexico City, Mexico, June 16-21, 2024*, pages 4336–4350. Association for Computational Linguistics, 2024. 8
- [2] Abdul Fatir Ansari, Jonathan Scarlett, and Harold Soh. A characteristic function approach to deep implicit generative modeling. In *2020 IEEE/CVF Conference on Computer Vision and Pattern Recognition, CVPR 2020, Seattle, WA, USA, June 13-19, 2020*, pages 7476–7484. Computer Vision Foundation / IEEE, 2020. 3
- [3] Martín Arjovsky, Soumith Chintala, and Léon Bottou. Wasserstein generative adversarial networks. In *Proceedings of the 34th International Conference on Machine Learning, ICML 2017, Sydney, NSW, Australia, 6-11 August 2017*, pages 214–223. PMLR, 2017. 2
- [4] Florian Brück. Generative neural networks for characteristic functions. *CoRR*, abs/2401.04778, 2024. 3
- [5] Nicolas Carion, Francisco Massa, Gabriel Synnaeve, Nicolas Usunier, Alexander Kirillov, and Sergey Zagoruyko. End-to-end object detection with transformers. In *Computer Vision - ECCV 2020 - 16th European Conference, Glasgow, UK, August 23-28, 2020, Proceedings, Part I*, pages 213–229. Springer, 2020. 1
- [6] George Cazenavette, Tongzhou Wang, Antonio Torralba, Alexei A. Efros, and Jun-Yan Zhu. Dataset distillation by matching training trajectories. In *IEEE/CVF Conference on Computer Vision and Pattern Recognition, CVPR 2022, New Orleans, LA, USA, June 18-24, 2022*, pages 10708–10717. IEEE, 2022. 2
- [7] Mark Chen, Jerry Tworek, Heewoo Jun, Qiming Yuan, Henrique Pondé de Oliveira Pinto, Jared Kaplan, Harri Edwards, Yuri Burda, Nicholas Joseph, Greg Brockman, Alex Ray, Raul Puri, Gretchen Krueger, Michael Petrov, Heidy Khlaaf, Girish Sastry, Pamela Mishkin, Brooke Chan, Scott Gray, Nick Ryder, Mikhail Pavlov, Alethea Power, Lukasz Kaiser, Mohammad Bavarian, Clemens Winter, Philippe Tillet, Felipe Petroski Such, Dave Cummings, Matthias Plappert, Fotios Chantzis, Elizabeth Barnes, Ariel Herbert-Voss, William Hebgen Guss, Alex Nichol, Alex Paino, Nikolas Tezak, Jie Tang, Igor Babuschkin, Suchir Balaji, Shantanu Jain, William Saunders, Christopher Hesse, Andrew N. Carr, Jan Leike, Joshua Achiam, Vedant Misra, Evan Morikawa, Alec Radford, Matthew Knight, Miles Brundage, Mira Murati, Katie Mayer, Peter Welinder, Bob McGrew, Dario Amodei, Sam McCandlish, Ilya Sutskever, and Wojciech Zaremba. Evaluating large language models trained on code. *CoRR*, abs/2107.03374, 2021. 1
- [8] Yutian Chen, Max Welling, and Alexander J. Smola. Super-samples from kernel herding. In *UAI 2010, Proceedings of*

- the Twenty-Sixth Conference on Uncertainty in Artificial Intelligence, Catalina Island, CA, USA, July 8-11, 2010*, pages 109–116. AUAI Press, 2010. 3
- [9] Kacper Chwialkowski, Aaditya Ramdas, Dino Sejdinovic, and Arthur Gretton. Fast two-sample testing with analytic representations of probability measures. In *Advances in Neural Information Processing Systems 28: Annual Conference on Neural Information Processing Systems 2015, December 7-12, 2015, Montreal, Quebec, Canada*, pages 1981–1989, 2015. 3
- [10] Mircea Cimpoi, Subhansu Maji, Iasonas Kokkinos, Sammy Mohamed, and Andrea Vedaldi. Describing textures in the wild. In *2014 IEEE Conference on Computer Vision and Pattern Recognition, CVPR 2014, Columbus, OH, USA, June 23-28, 2014*, pages 3606–3613. IEEE Computer Society, 2014. 2
- [11] William Cook. A hierarchical decomposition of kullback-leibler divergence: Disentangling marginal mismatches from statistical dependencies. *CoRR*, abs/2504.09029, 2025. 2
- [12] Alexey Dosovitskiy, Lucas Beyer, Alexander Kolesnikov, Dirk Weissenborn, Xiaohua Zhai, Thomas Unterthiner, Mostafa Dehghani, Matthias Minderer, Georg Heigold, Sylvain Gelly, Jakob Uszkoreit, and Neil Houlsby. An image is worth 16x16 words: Transformers for image recognition at scale. In *9th International Conference on Learning Representations, ICLR 2021, Virtual Event, Austria, May 3-7, 2021*. OpenReview.net, 2021. 1
- [13] T.W. Epps and Kenneth J. Singleton. An omnibus test for the two-sample problem using the empirical characteristic function. *Journal of Statistical Computation and Simulation*, 26(3-4):177–203, 1986. 3
- [14] V. Alba Fernández, María-Dolores Jiménez-Gamero, and Joaquín Muñoz-García. A test for the two-sample problem based on empirical characteristic functions. *Comput. Stat. Data Anal.*, 52(7):3730–3748, 2008. 3
- [15] Leo Gao, Stella Biderman, Sid Black, Laurence Golding, Travis Hoppe, Charles Foster, Jason Phang, Horace He, Anish Thite, Noa Nabeshima, Shawn Presser, and Connor Leahy. The pile: An 800gb dataset of diverse text for language modeling. *CoRR*, abs/2101.00027, 2021. 1
- [16] Arthur Gretton, Karsten M. Borgwardt, Malte J. Rasch, Bernhard Schölkopf, and Alexander J. Smola. A kernel two-sample test. *J. Mach. Learn. Res.*, 13:723–773, 2012. 2
- [17] Rishabh K. Iyer, Ninad Khargoankar, Jeff A. Bilmes, and Himanshu Asanani. Submodular combinatorial information measures with applications in machine learning. In *Algorithmic Learning Theory, 16-19 March 2021, Virtual Conference, Worldwide*, pages 722–754. PMLR, 2021. 1
- [18] John Jumper, Richard Evans, Alexander Pritzel, Tim Green, Michael Figurnov, Olaf Ronneberger, Kathryn Tunyasuvunakool, Russ Bates, Augustin Žídek, Anna Potapenko, Alex Bridgland, Clemens Meyer, Simon A. A. Kohl, Andrew J. Ballard, Andrew Cowie, Bernardino Romera-Paredes, Stanislav Nikolov, Rishub Jain, Jonas Adler, Trevor Back, Stig Petersen, David Reiman, Ellen Clancy, Michal Zielinski, Martin Steinegger, Michalina Pacholska, Tamas Berghammer, Sebastian Bodenstern, David Silver, Oriol Vinyals, Andrew W. Senior, Koray Kavukcuoglu, Pushmeet Kohli, and Demis Hassabis. Highly accurate protein structure prediction with AlphaFold. *Nature*, 596(7873):583–589, 2021. 1
- [19] KrishnaTeja Killamsetty, Durga Sivasubramanian, Ganesh Ramakrishnan, Abir De, and Rishabh K. Iyer. GRAD-MATCH: gradient matching based data subset selection for efficient deep model training. In *Proceedings of the 38th International Conference on Machine Learning, ICML 2021, 18-24 July 2021, Virtual Event*, pages 5464–5474. PMLR, 2021. 1, 3
- [20] KrishnaTeja Killamsetty, Durga Sivasubramanian, Ganesh Ramakrishnan, and Rishabh K. Iyer. GLISTER: generalization based data subset selection for efficient and robust learning. In *Thirty-Fifth AAAI Conference on Artificial Intelligence, AAAI 2021, Thirty-Third Conference on Innovative Applications of Artificial Intelligence, IAAI 2021, The Eleventh Symposium on Educational Advances in Artificial Intelligence, EAAI 2021, Virtual Event, February 2-9, 2021*, pages 8110–8118. AAAI Press, 2021. 3
- [21] Diederik P. Kingma and Max Welling. Auto-encoding variational bayes. In *2nd International Conference on Learning Representations, ICLR 2014, Banff, AB, Canada, April 14-16, 2014, Conference Track Proceedings*, 2014. 2
- [22] Alex Krizhevsky, Ilya Sutskever, and Geoffrey E. Hinton. Imagenet classification with deep convolutional neural networks. In *Advances in Neural Information Processing Systems 25: 26th Annual Conference on Neural Information Processing Systems 2012. Proceedings of a meeting held December 3-6, 2012, Lake Tahoe, Nevada, United States*, pages 1106–1114, 2012. 2
- [23] Dong Bok Lee, Seanie Lee, Joonho Ko, Kenji Kawaguchi, Juho Lee, and Sung Ju Hwang. Self-supervised dataset distillation for transfer learning. In *The Twelfth International Conference on Learning Representations, ICLR 2024, Vienna, Austria, May 7-11, 2024*. OpenReview.net, 2024. 1
- [24] Yujia Li, David H. Choi, Junyoung Chung, Nate Kushman, Julian Schrittwieser, Rémi Leblond, Tom Eccles, James Keeling, Felix Gimeno, Agustin Dal Lago, Thomas Hubert, Peter Choy, Cyprien de Masson d’Autume, Igor Babuschkin, Xinyun Chen, Po-Sen Huang, Johannes Welbl, Sven Gowal, Alexey Cherepanov, James Molloy, Daniel J. Mankowitz, Esme Sutherland Robson, Pushmeet Kohli, Nando de Freitas, Koray Kavukcuoglu, and Oriol Vinyals. Competition-level code generation with alphacode. *CoRR*, abs/2203.07814, 2022. 1
- [25] Tsung-Yi Lin, Michael Maire, Serge J. Belongie, James Hays, Pietro Perona, Deva Ramanan, Piotr Dollár, and C. Lawrence Zitnick. Microsoft COCO: common objects in context. In *Computer Vision - ECCV 2014 - 13th European Conference, Zurich, Switzerland, September 6-12, 2014, Proceedings, Part V*, pages 740–755. Springer, 2014. 1
- [26] Ze Liu, Yutong Lin, Yue Cao, Han Hu, Yixuan Wei, Zheng Zhang, Stephen Lin, and Baining Guo. Swin transformer: Hierarchical vision transformer using shifted windows. In *2021 IEEE/CVF International Conference on Computer Vi-*

- tion, *ICCV 2021, Montreal, QC, Canada, October 10-17, 2021*, pages 9992–10002. IEEE, 2021. 1
- [27] Leland McInnes and John Healy. UMAP: uniform manifold approximation and projection for dimension reduction. *CoRR*, abs/1802.03426, 2018. 3
- [28] Amil Merchant, Simon L. Batzner, Samuel S. Schoenholz, Muratahan Aykol, Gowoon Cheon, and Ekin Dogus Cubuk. Scaling deep learning for materials discovery. *Nat.*, 624 (7990):80–85, 2023. 1
- [29] Baharan Mirzasoleiman, Jeff A. Bilmes, and Jure Leskovec. Coresets for data-efficient training of machine learning models. In *Proceedings of the 37th International Conference on Machine Learning, ICML 2020, 13-18 July 2020, Virtual Event*, pages 6950–6960. PMLR, 2020. 1
- [30] Seyed-Mohsen Moosavi-Dezfooli, Alhussein Fawzi, and Pascal Frossard. Deepfool: A simple and accurate method to fool deep neural networks. In *2016 IEEE Conference on Computer Vision and Pattern Recognition, CVPR 2016, Las Vegas, NV, USA, June 27-30, 2016*, pages 2574–2582. IEEE Computer Society, 2016. 3
- [31] Erik Nijkamp, Bo Pang, Hiroaki Hayashi, Lifu Tu, Huan Wang, Yingbo Zhou, Silvio Savarese, and Caiming Xiong. Codegen: An open large language model for code with multi-turn program synthesis. In *The Eleventh International Conference on Learning Representations, ICLR 2023, Kigali, Rwanda, May 1-5, 2023*. OpenReview.net, 2023. 1
- [32] Mansheej Paul, Surya Ganguli, and Gintare Karolina Dziugaite. Deep learning on a data diet: Finding important examples early in training. In *Advances in Neural Information Processing Systems 34: Annual Conference on Neural Information Processing Systems 2021, NeurIPS 2021, December 6-14, 2021, virtual*, pages 20596–20607, 2021. 3
- [33] Sylvestre-Alvise Rebuffi, Alexander Kolesnikov, Georg Sperl, and Christoph H. Lampert. icarl: Incremental classifier and representation learning. In *2017 IEEE Conference on Computer Vision and Pattern Recognition, CVPR 2017, Honolulu, HI, USA, July 21-26, 2017*, pages 5533–5542. IEEE Computer Society, 2017. 1
- [34] Donald Richards. Distance correlation: A new tool for detecting association and measuring correlation between data sets, 2017. 2
- [35] Olga Russakovsky, Jia Deng, Hao Su, Jonathan Krause, Sanjeev Satheesh, Sean Ma, Zhiheng Huang, Andrej Karpathy, Aditya Khosla, Michael S. Bernstein, Alexander C. Berg, and Li Fei-Fei. Imagenet large scale visual recognition challenge. *Int. J. Comput. Vis.*, 115(3):211–252, 2015. 1
- [36] Ozan Sener and Silvio Savarese. Active learning for convolutional neural networks: A core-set approach. In *6th International Conference on Learning Representations, ICLR 2018, Vancouver, BC, Canada, April 30 - May 3, 2018, Conference Track Proceedings*. OpenReview.net, 2018. 3
- [37] Rohan Taori, Ishaan Gulrajani, Tianyi Zhang, Yann Dubois, Xuechen Li, Carlos Guestrin, Percy Liang, and Tatsunori Hashimoto. Alpaca: A strong, replicable instruction-following model, 2023. Stanford Center for Research on Foundation Models (CRFM). 8
- [38] Hugo Touvron, Thibaut Lavril, Gautier Izacard, Xavier Martinet, Marie-Anne Lachaux, Timothée Lacroix, Baptiste Rozière, Naman Goyal, Eric Hambro, Faisal Azhar, Aurélien Rodriguez, Armand Joulin, Edouard Grave, and Guillaume Lample. Llama: Open and efficient foundation language models. *CoRR*, abs/2302.13971, 2023. 8
- [39] Pascal Vincent, Hugo Larochelle, Yoshua Bengio, and Pierre-Antoine Manzagol. Extracting and composing robust features with denoising autoencoders. In *Machine Learning, Proceedings of the Twenty-Fifth International Conference (ICML 2008), Helsinki, Finland, June 5-9, 2008*, pages 1096–1103. ACM, 2008. 2
- [40] Catherine Wah, Steve Branson, Peter Welinder, Pietro Perona, and Serge Belongie. Caltech-ucsd birds-200-2011 dataset. Technical Report CNS-TR-2011-001, California Institute of Technology, 2011. 9
- [41] Shaobo Wang, Yicun Yang, Zhiyuan Liu, Chenghao Sun, Xuming Hu, Conghui He, and Linfeng Zhang. Dataset distillation with neural characteristic function: A minmax perspective. In *IEEE/CVF Conference on Computer Vision and Pattern Recognition, CVPR 2025, Nashville, TN, USA, June 11-15, 2025*, pages 25570–25580. Computer Vision Foundation / IEEE, 2025. 1, 2, 3, 9
- [42] Fuping Wu and Xiahai Zhuang. CF distance: A new domain discrepancy metric and application to explicit domain adaptation for cross-modality cardiac image segmentation. *IEEE Trans. Medical Imaging*, 39(12):4274–4285, 2020. 3
- [43] Jaehong Yoon, Divyam Madaan, Eunho Yang, and Sung Ju Hwang. Online coreset selection for rehearsal-based continual learning. In *The Tenth International Conference on Learning Representations, ICLR 2022, Virtual Event, April 25-29, 2022*. OpenReview.net, 2022. 1
- [44] Jie You, Jae-Won Chung, and Mosharaf Chowdhury. Zeus: Understanding and optimizing GPU energy consumption of DNN training. In *USENIX NSDI*, 2023. 6
- [45] Bo Zhao and Hakan Bilen. Dataset condensation with distribution matching. In *IEEE/CVF Winter Conference on Applications of Computer Vision, WACV 2023, Waikoloa, HI, USA, January 2-7, 2023*, pages 6503–6512. IEEE, 2023. 1, 2
- [46] Bo Zhao, Konda Reddy Mopuri, and Hakan Bilen. Dataset condensation with gradient matching. In *9th International Conference on Learning Representations, ICLR 2021, Virtual Event, Austria, May 3-7, 2021*. OpenReview.net, 2021. 1, 2
- [47] Boran Zhao, Haiduo Huang, Qiwei Dang, Wenzhe Zhao, Tian Xia, and Pengju Ren. NMS: efficient edge DNN training via near-memory sampling on manifolds. *CoRR*, abs/2508.02313, 2025. 3
- [48] Yongchao Zhou, Ehsan Nezhadarya, and Jimmy Ba. Dataset distillation using neural feature regression. In *Advances in Neural Information Processing Systems 35: Annual Conference on Neural Information Processing Systems 2022, NeurIPS 2022, New Orleans, LA, USA, November 28 - December 9, 2022*, 2022. 2

# Supplementary Material

## A. Computational Overhead

| Module/Eq.             | Complexity/ $O(\cdot)$  | Total FLOPs                   | Peak RAM       |
|------------------------|-------------------------|-------------------------------|----------------|
| Graph Construction (1) | $N_c^2 \cdot D$         | $7.41 \times 10^{14}$         | <b>778 MB</b>  |
| Spectral Embedding (2) | $N_c^3$                 | $2.10 \times 10^{12}$         | 163 KB         |
| Cost Matrix (3)        | $M_c \cdot N_c \cdot d$ | $6.30 \times 10^{12}$         | 655 KB         |
| Hungarian Match        | $M_c \cdot N_c^2$       | $8.40 \times 10^{13}$         | 741 KB         |
| PD-CFD Loss (9)        | $(N_c + M_c)N_{freq}d$  | $9.20 \times 10^{12}$         | 1.03 MB        |
| <b>Total FAST</b>      | –                       | $8.43 \times 10^{14} \approx$ | <b>782 MB</b>  |
| ResNet-50 Comparison   | –                       | $5.25 \times 10^{15} \approx$ | <b>6.25 GB</b> |

Table 3. Expensive Computation Breakdown on ImageNet-1K. **Note:** FAST assumes per-class selection. ResNet-50 FLOPs are for one epoch inference on ImageNet-1K with a batch size of 256. Total feature extraction overhead of FAST on ImageNet-1K is 16% of ResNet-50.

| Keep Rate                  | 10%         | Time(h)    | 20%         | Time(h)    | 30%         | Time(h)    | Full |
|----------------------------|-------------|------------|-------------|------------|-------------|------------|------|
| previous SOTA <sup>‡</sup> | 53.6        | 7.9        | 62.6        | 21.1       | 64.5        | 30.2       | 71.2 |
| FAST <sup>‡</sup>          | <b>56.2</b> | <b>2.5</b> | <b>63.9</b> | <b>6.1</b> | <b>66.9</b> | <b>8.2</b> | 71.2 |

Table 4. Performance Comparison on ImageNet-1K. <sup>‡</sup>On CPU.

## B. Optimization Stability

The *Hungarian mapping* evolves from dynamic exploration to stable anchoring, ensuring robust continuous-to-discrete alignment. Despite discrete updates to  $\pi$ , the loss maintains continuity at cost-equalizing *Voronoi boundaries*, and divergence is prevented by topological constraints that limit gradient fluctuations to the local manifold neighborhood. Since *Hungarian algorithm* minimizes the transport cost globally, gradient descent on the smooth objective  $\tilde{Y}$  ensures  $\mathcal{L}(\tilde{Y}^{(t+1)}, \pi^{(t+1)}) \leq \mathcal{L}(\tilde{Y}^{(t)}, \pi^{(t)})$ , yielding monotonic descent optimization:  $0 \leq \mathcal{L}_{total}^{(t+1)} \leq \mathcal{L}_{total}^{(t)}$ , where *Monotone Convergence Theorem* guarantees convergence.

## C. Necessity of Embeddings

In LLM experiments, we utilize general Sentence-BERT embeddings as standard preprocessing for manifold construction. The structural distinction between the encoder-only embedder and decoder-only LLM introduces a general semantic prior rather than coupled architectural bias, confirmed by Table 5 that shows FAST’s robust generalization.

| Model   | L-FAST                       | L-Rand                           | Q-FAST                       | Q-Rand                           | M-FAST                       | M-Rand                           |
|---------|------------------------------|----------------------------------|------------------------------|----------------------------------|------------------------------|----------------------------------|
| Acc (%) | 39.0 <sup>†</sup> <b>8.7</b> | 35.9 <sup>†</sup> <sub>5.6</sub> | 72.3 <sup>†</sup> <b>6.1</b> | 70.9 <sup>†</sup> <sub>4.7</sub> | 63.1 <sup>†</sup> <b>4.0</b> | 61.6 <sup>†</sup> <sub>2.5</sub> |

**Notation:** L: LLaMA2-7B, Q: Qwen2.5-7B, M: Mistral-7B, Rand:Random. <sup>†</sup> indicates the relative improvement to the base model.

Table 5. Supplementary Experiments on LLM datasets.

## D. More Ablation Studies

Use CIFAR-10 dataset (10% KR, training ResNet-18) unless noted; random sampling shows  $75.70\%_{\pm 7.63}$  accuracy.

| Method                 | Acc (%)      | Time (s)   | Energy (Wh)  | Std         | Opt/Steps |
|------------------------|--------------|------------|--------------|-------------|-----------|
| Pixel-Opt <sup>‡</sup> | 61.52        | 3770       | 29.75        | 13.73       | 1300      |
| ResNet-50 <sup>†</sup> | 81.51        | 627.67     | 37.75        | 3.32        | 230       |
| FAST <sup>‡</sup>      | <b>90.32</b> | <b>353</b> | <b>1.409</b> | <b>1.21</b> | <b>80</b> |

Table 6. Graph Feature Extractor Ablation on <sup>‡</sup>CPU, <sup>†</sup>GPU.

**Analysis:** Pixel-level optimization fails due to the sparsity and noise of high-dimensional space, while incurring massive computational costs (10× slower). ResNet-50 features suffer from architectural bias and computational overhead.

| Parameter       | Ours                              | $k = 5$          | $k = 50$         | $d = 8$          | $d = 128$          |
|-----------------|-----------------------------------|------------------|------------------|------------------|--------------------|
| Trustworthiness | <b>0.95<math>\pm 0.01</math></b>  | 0.73 $\pm 0.10$  | 0.52 $\pm 0.09$  | 0.44 $\pm 0.09$  | 0.92 $\pm 0.02$    |
| Continuity      | 0.91 $\pm 0.03$                   | 0.49 $\pm 0.15$  | 0.93 $\pm 0.06$  | 0.92 $\pm 0.03$  | 0.87 $\pm 0.06$    |
| Acc (%)         | <b>90.32<math>\pm 1.21</math></b> | 72.12 $\pm 5.56$ | 85.01 $\pm 3.27$ | 78.86 $\pm 3.13$ | 86.73 $\pm 4.16^*$ |

Table 7. Hyperparameter Ablation (neighbor scale  $k$  and reduced dimension  $d$ ). \*Time doubles. FAST adopts  $k = 15$  and  $d = 32$ .

**Analysis:** Small  $k$  fractures the manifold, while large  $k$  causes collapse, connecting distant classes; low  $d$  bottlenecks information, and high  $d$  adds noise and doubles optimization time. Our settings optimally preserve topology.

| Strategy  | DAS              | PES              | PUS              | US               | Collinear        | PDAS                              |
|-----------|------------------|------------------|------------------|------------------|------------------|-----------------------------------|
| Acc (%)   | 88.89 $\pm 2.23$ | 87.12 $\pm 2.60$ | 88.66 $\pm 2.01$ | 86.60 $\pm 2.73$ | 74.16 $\pm 7.77$ | <b>90.32<math>\pm 1.21</math></b> |
| Opt/Steps | 150              | 400              | 250              | 430              | 100*             | <b>80</b>                         |

Table 8. Impact of Frequency Selection. \*Optimization failure mode. Illustration and abbreviations, please refer to paper Fig. 9.

**Analysis:** Baselines unstably converge due to suboptimal frequency selection; PDAS achieves optimal stability by progressively selecting discriminative frequencies.

| Method       | CIFAR-10                          | RESISC-45                         | DTD                               |
|--------------|-----------------------------------|-----------------------------------|-----------------------------------|
| FAST-Vanilla | 88.17 $\pm 2.12$                  | 82.01 $\pm 3.99$                  | 41.15 $\pm 3.20$                  |
| FAST-PD      | <b>90.32<math>\pm 1.21</math></b> | <b>85.00<math>\pm 2.01</math></b> | <b>45.77<math>\pm 2.53</math></b> |

Table 9. Phase-Decoupled CFD Ablation (full ablation in Fig. 7).

**Analysis:** *CFD* fails to capture high-frequency details due to amplitude-phase coupling. *PD-CFD* resolves this, showing substantial gains on texture-rich DTD (+4.62%) and RESISC-45 (+2.99%) compared to CIFAR-10 (+2.15%).

## E. Additional Analysis on Limitations of KL and CE for High-Order Moment Alignment

**Notation.** Let  $P$  be an unknown target distribution on  $\mathcal{X} \subseteq \mathbb{R}^d$  with density  $p$ . An exponential family is

$$\mathcal{Q}_T := \left\{ q_\theta(x) = h(x) \exp(\theta^\top T(x) - A(\theta)) \mid \theta \in \Theta \subset \mathbb{R}^m \right\},$$

where  $T : \mathcal{X} \rightarrow \mathbb{R}^m$  is a vector of sufficient statistics,  $A(\theta) := \log \int h(x) \exp(\theta^\top T(x)) dx$  is the log-partition function (cumulant generating function), and  $h$  is a base

density. We write  $\mu(\theta) := \nabla A(\theta) = \mathbb{E}_{Q_\theta}[T(X)]$  for the mean-parameter map.

For  $k \in \mathbb{N}$ , define the (truncated) polynomial statistics

$$T^{(\leq k)}(x) = (x, xx^\top, x^{\otimes 3}, \dots, x^{\otimes k}),$$

so that  $\mathcal{Q}_{\leq k}$  denotes the exponential family whose sufficient statistics are all monomials up to degree  $k$  (with a suitable choice of  $h$  to ensure normalizability).

**Proposition 1** (I-projection yields moment matching on the chosen statistics). *Consider the KL minimization (I-projection) of  $P$  onto an exponential family  $\mathcal{Q}_T$ :*

$$\begin{aligned} \theta^* &\in \arg \min_{\theta \in \Theta} D_{\text{KL}}(P \parallel Q_\theta) \\ &= \arg \min_{\theta} \int p(x) \log \frac{p(x)}{q_\theta(x)} dx. \end{aligned} \quad (17)$$

*Then  $A$  is convex and the KL objective is strictly convex in  $\theta$  on the mean-parameter interior; the unique minimizer  $\theta^*$  (when it exists) satisfies the first-order optimality condition*

$$\nabla_\theta \left( \mathbb{E}_P[\theta^\top T(X)] - A(\theta) \right) \Big|_{\theta=\theta^*} = \mathbb{E}_P[T(X)] - \nabla A(\theta^*) = 0.$$

*Equivalently,*

$$\mathbb{E}_P[T(X)] = \mathbb{E}_{Q_{\theta^*}}[T(X)].$$

*Proof (via convex duality and Fenchel–Legendre conjugacy).* Expanding the KL divergence,

$$D_{\text{KL}}(P \parallel Q_\theta) = -H(P) - \mathbb{E}_P[\theta^\top T(X) - A(\theta) + \log h(X)],$$

where  $H(P)$  and  $\mathbb{E}_P[\log h(X)]$  are  $\theta$ -independent constants. Thus minimizing  $D_{\text{KL}}(P \parallel Q_\theta)$  is equivalent to maximizing the concave functional

$$\mathcal{L}(\theta) := \mathbb{E}_P[\theta^\top T(X)] - A(\theta).$$

Since  $A$  is convex (indeed,  $A$  is the log-moment generating function of  $T$  under  $h$ ),  $\mathcal{L}$  is concave and (under standard interiority conditions) has a unique maximizer  $\theta^*$ . The Fenchel–Legendre conjugate of  $A$  is  $A^*(\mu) := \sup_\theta \{\langle \theta, \mu \rangle - A(\theta)\}$ ; strong duality yields that the optimal  $\theta^*$  satisfies  $\nabla A(\theta^*) = \mu^* = \mathbb{E}_P[T(X)]$  (i.e. the moment-matching equations). Finally  $\nabla A(\theta) = \mathbb{E}_{Q_\theta}[T(X)]$  by standard exponential-family calculus, completing the proof.  $\square$

**Corollary 1** (Distributions controlled by KL under restricted sufficient statistics). *Let  $\mathcal{Q}_T$  be any exponential family with sufficient statistics  $T$ . Then the I-projection  $Q_{\theta^*}$  aligns exactly those coordinates of  $T$ :*

$$\mathbb{E}_P[T_i(X)] = \mathbb{E}_{Q_{\theta^*}}[T_i(X)] \quad \text{for each component } T_i,$$

*but imposes no necessary constraint on expectations of functions  $f$  lying outside the linear span of  $\{1, T_1, \dots, T_m\}$ . In particular, if  $T = T^{(\leq k)}$  contains all monomials up to degree  $k$ , then KL minimization guarantees matching of all raw moments up to order  $k$ , and does not in general constrain any  $(k+1)$ -st or higher-order moments.*

*Proof.* Immediate from Proposition 1, noting that the optimality system is exactly the linear system matching  $\mathbb{E}_P[T]$  and  $\mathbb{E}_{Q_\theta}[T]$ . Any  $f$  outside the closed linear span of  $\{1, T\}$  cannot be represented as  $\alpha_0 + \alpha^\top T$ , hence its expectation is unconstrained by the KKT system.  $\square$

**Corollary 2** (Gaussian family ( $k = 2$ ) controls mean and covariance but not higher cumulants). *Let  $\mathcal{Q}_\mathcal{N} = \{\mathcal{N}(\mu, \Sigma)\}$ . Then  $\mathcal{Q}_\mathcal{N}$  is an exponential family with  $T(x) = (x, xx^\top)$  and  $\nabla A(\mu, \Sigma) = (\mathbb{E}[X], \mathbb{E}[XX^\top])$ . The I-projection  $Q_{\theta^*} = \mathcal{N}(\mu^*, \Sigma^*)$  thus satisfies*

$$\mathbb{E}_{Q_{\theta^*}}[X] = \mathbb{E}_P[X], \quad \mathbb{E}_{Q_{\theta^*}}[XX^\top] = \mathbb{E}_P[XX^\top],$$

*but neither skewness (third cumulant) nor kurtosis (fourth cumulant) is constrained or minimized by the KL objective in general.*

*Proof.* A direct specialization of Corollary 1 with  $k = 2$ .  $\square$

**Proposition 2** (Augmenting statistics raises the matched moment order, but only up to that order). *Let  $\mathcal{Q}_{\leq k}$  denote the exponential family with  $T^{(\leq k)}$ . Then the sequence of I-projections  $\{Q^{(k)}\}_{k \geq 1}$  defined by*

$$Q^{(k)} \in \arg \min_{Q \in \mathcal{Q}_{\leq k}} D_{\text{KL}}(P \parallel Q)$$

*satisfies, for each fixed  $k$ ,*

$$\mathbb{E}_{Q^{(k)}}[X^{\otimes r}] = \mathbb{E}_P[X^{\otimes r}] \quad \text{for all } r = 1, 2, \dots, k,$$

*and there is no general guarantee that  $\mathbb{E}_{Q^{(k)}}[X^{\otimes r}]$  aligns with  $\mathbb{E}_P[X^{\otimes r}]$  for any  $r > k$ .*

*Proof.* By Proposition 1 applied to  $T^{(\leq k)}$ , the optimality conditions enforce equality of the first  $k$  raw-moment tensors. Since the KL objective reduces to a linear functional of  $T$  minus  $A(\theta)$ , any statistics not included in  $T$  do not appear in the optimality system and remain uncontrolled.  $\square$

**Remark 1** (Consequences for KL/CE-based evaluation of distributional alignment). *Since cross-entropy minimization is equivalent to minimizing  $D_{\text{KL}}(P \parallel Q_\theta)$  when  $P$  is fixed, Propositions 1–2 imply a fundamental limitation: Under a*

restricted exponential family, KL/CE can certify alignment of at most the moments encoded in  $T$  (e.g., mean and covariance for Gaussians), and it provides no guarantees for higher-order moments or cumulants that are not present in  $T$ . Hence, unless higher-order statistics are explicitly included in the model (i.e., increasing  $k$ ), KL/CE-based fitting and evaluation do not ensure moment alignment.

**Example 1** (Gaussian vs. heavy-tailed target: kurtosis mismatch at the KL optimum). Let  $P$  be a zero-mean heavy-tailed distribution (e.g., a centered Laplace in 1D) with variance  $\sigma^2$  and kurtosis  $\kappa_P > 3$ . Its I-projection onto  $\mathcal{Q}_{\mathcal{N}}$  is  $Q^* = \mathcal{N}(0, \sigma^2)$ , which matches mean and variance by Corollary 2. However,  $\kappa_{Q^*} = 3 \neq \kappa_P$ , i.e., fourth-order moments are not aligned at the KL optimum—a concrete manifestation of Remark 1.

**Remark 2** (Mixtures vs. single exponential families). A Gaussian mixture model (GMM) is a convex combination of Gaussians and not a single exponential family with a fixed finite-dimensional  $T$ . Therefore, the structural limitation in Propositions 1–2 does not apply in the same form to GMMs: with sufficiently many components, a GMM can approximate higher-order structures arbitrarily well. However, practical optimization remains nonconvex and capacity-limited, so alignment may still fail in practice despite the absence of a finite-dimensional  $T$ .

### A General Counterexample: Small KL yet Divergent Higher-Order Moments

We now give a short, self-contained construction showing that (beyond model restrictions) the KL divergence itself does not control unbounded test-function expectations, such as moments.

**Proposition 3** (KL can be arbitrarily small while  $k$ -th moments diverge). Fix any integer  $k \geq 3$ . There exists a sequence of distributions  $P_M$  and a reference  $Q$  such that

$$D_{\text{KL}}(P_M \| Q) \rightarrow 0 \quad \text{but} \quad |\mathbb{E}_{P_M}[X^k] - \mathbb{E}_Q[X^k]| \rightarrow \infty.$$

*Proof.* Let  $Q = \mathcal{N}(0, 1)$  and  $R_M = \mathcal{N}(M, 1)$ . Define the mixture

$$P_M = (1 - \varepsilon_M) Q + \varepsilon_M R_M, \quad \varepsilon_M = \frac{1}{M^2 \log M}.$$

(i) *KL upper bound by joint convexity.* By convexity of  $D_{\text{KL}}(\cdot \| Q)$  in its first argument,

$$\begin{aligned} D_{\text{KL}}(P_M \| Q) &\leq (1 - \varepsilon_M) D_{\text{KL}}(Q \| Q) + \varepsilon_M D_{\text{KL}}(R_M \| Q) \\ &= \varepsilon_M \cdot \frac{M^2}{2} = \frac{1}{2 \log M} \rightarrow 0, \end{aligned} \tag{18}$$

where  $D_{\text{KL}}(\mathcal{N}(M, 1) \| \mathcal{N}(0, 1)) = \frac{M^2}{2}$ .

(ii) *Divergence of the  $k$ -th moment gap.* For  $k \geq 3$ ,  $\mathbb{E}_{R_M}[X^k] \sim M^k$ . Hence

$$\begin{aligned} |\mathbb{E}_{P_M}[X^k] - \mathbb{E}_Q[X^k]| &= \varepsilon_M |\mathbb{E}_{R_M}[X^k] - \mathbb{E}_Q[X^k]| \\ &\gtrsim \varepsilon_M M^k = \frac{M^{k-2}}{\log M} \xrightarrow{M \rightarrow \infty} \infty. \end{aligned} \tag{19}$$

Thus KL can be made arbitrarily small while the  $k$ -th moment discrepancy diverges.  $\square$

**Interpretation.** Pinsker’s inequality controls only bounded test functions via total variation; polynomial moments are unbounded, so small KL does not imply closeness of higher moments. Proposition 3 complements the structural limitation (Propositions 1–2) by showing a metric limitation: even without any modeling restrictions, KL does not bound higher-order moments.

### F. Limitations of MMD for Aligning Higher-Order Statistics

Maximum Mean Discrepancy (MMD) is widely used as a nonparametric distributional metric, defined for a positive definite kernel  $k$  by

$$\begin{aligned} \text{MMD}_k(P, Q) &= \|\mu_P - \mu_Q\|_{\mathcal{H}_k} \\ &= \sup_{\|f\|_{\mathcal{H}_k} \leq 1} (\mathbb{E}_P[f(X)] - \mathbb{E}_Q[f(X)]), \end{aligned} \tag{20}$$

where  $\mathcal{H}_k$  is the reproducing kernel Hilbert space (RKHS) associated with  $k$ . When  $k$  is characteristic, MMD metrizes weak convergence. However, for the purpose of coreset selection—where the objective is to align *all* statistical moments (including heavy-tailed or high-order cumulants)—weak convergence is insufficient. We show below that with commonly used bounded kernels (e.g., Gaussian, Laplacian), MMD does *not* control higher-order moments, even when  $\text{MMD}_k(P, Q)$  is arbitrarily small.

**Setup.** Let  $k(x, y)$  be any bounded positive definite kernel with  $\sup_{x, y} |k(x, y)| \leq K < \infty$  (this includes the Gaussian RBF). Let  $Q$  be any reference distribution with finite moments of all orders.

We construct the following sequence:

$$P_M = (1 - \varepsilon_M) Q + \varepsilon_M R_M,$$

where  $R_M$  is a distribution concentrated at radius  $\|x\| \approx M$ , and  $\varepsilon_M$  is a vanishing mixing weight.

The construction is analogous to the KL example in Proposition 3 but adapted to the MMD geometry.

**Proposition 4** (Small MMD does not control higher-order moments). *For any bounded kernel  $k$  and any integer  $r \geq 3$ , there exists a sequence  $P_M$  such that*

$$\text{MMD}_k(P_M, Q) \rightarrow 0 \quad \text{but} \quad |\mathbb{E}_{P_M}[X^r] - \mathbb{E}_Q[X^r]| \rightarrow \infty.$$

*Proof.* Because  $k$  is bounded, the RKHS norm of the kernel mean embedding satisfies

$$\|\mu_{P_M} - \mu_Q\|_{\mathcal{H}_k} \leq \mathbb{E}_{P_M, Q}[|k(X, Y)|] \leq K.$$

More precisely,

$$\mu_{P_M} = (1 - \varepsilon_M)\mu_Q + \varepsilon_M\mu_{R_M},$$

hence

$$\text{MMD}_k(P_M, Q) = \varepsilon_M \|\mu_{R_M} - \mu_Q\|_{\mathcal{H}_k} \leq 2K \varepsilon_M.$$

Taking  $\varepsilon_M = 1/\log M$  yields

$$\text{MMD}_k(P_M, Q) \leq \frac{2K}{\log M} \xrightarrow{M \rightarrow \infty} 0.$$

Next, choose  $R_M$  such that almost all its mass lies on  $\|x\| \approx M$ . Then the  $r$ -th moment satisfies

$$\mathbb{E}_{R_M}[X^r] \asymp M^r,$$

and therefore

$$\begin{aligned} \mathbb{E}_{P_M}[X^r] &= (1 - \varepsilon_M)\mathbb{E}_Q[X^r] + \varepsilon_M \mathbb{E}_{R_M}[X^r] \\ &\asymp \mathbb{E}_Q[X^r] + \varepsilon_M M^r. \end{aligned} \quad (21)$$

Since  $\varepsilon_M M^r = M^r / \log M \rightarrow \infty$  for any  $r \geq 3$ , we obtain

$$|\mathbb{E}_{P_M}[X^r] - \mathbb{E}_Q[X^r]| \rightarrow \infty,$$

even while  $\text{MMD}_k(P_M, Q) \rightarrow 0$ .  $\square$

**Interpretation.** This result parallels Proposition 3 for KL: both reveal a *metric limitation* independent of modeling assumptions. For bounded kernels, MMD metrizes weak convergence but cannot control expectations of unbounded test functions—particularly polynomial functions that capture higher-order moments, tail behavior, or heavy-tailed anisotropy.

Consequently, when MMD is used as an objective for coreset construction, moment alignment depends critically on the expressiveness of the chosen kernel. If the kernel is insufficient to probe heavy tails or high-order interactions, the resulting coreset may perfectly match the MMD score yet deviate drastically in higher-order statistics—precisely the regime where our PD-CFD metric provides a more faithful discrepancy measure.

## G. Characteristic Functions: Complete Statistical Representation and Fourier–Analytic Foundations

**Notation.** Let  $P$  be a Borel probability measure on  $\mathbb{R}^d$  with random vector  $X \sim P$ . The *characteristic function* (CF) of  $P$  is

$$\varphi_P(\omega) := \int_{\mathbb{R}^d} e^{i\omega^\top x} P(dx) = \mathbb{E}_P[e^{i\omega^\top X}], \quad \omega \in \mathbb{R}^d.$$

Each  $\varphi_P$  is bounded ( $|\varphi_P| \leq 1$ ), uniformly continuous, and positive definite.

**Proposition 5** (Fourier inversion: recovering  $P$  from  $\varphi_P$ ). *Suppose  $P$  admits a density  $p \in L^1(\mathbb{R}^d)$ . Then  $p$  can be recovered from its characteristic function by the inverse Fourier transform:*

$$p(x) = \frac{1}{(2\pi)^d} \int_{\mathbb{R}^d} e^{-i\omega^\top x} \varphi_P(\omega) d\omega, \quad \text{for a.e. } x \in \mathbb{R}^d.$$

*More generally, for any  $f \in L^1(\mathbb{R}^d)$  with Fourier transform  $\hat{f}(\omega) := \int e^{i\omega^\top x} f(x) dx$ ,*

$$\int_{\mathbb{R}^d} f(x) P(dx) = \frac{1}{(2\pi)^d} \int_{\mathbb{R}^d} \hat{f}(\omega) \varphi_P(\omega) d\omega.$$

*Thus, the knowledge of  $\varphi_P$  on  $\mathbb{R}^d$  uniquely determines all integrals  $\int f dP$ , and hence the measure  $P$  itself.*

*Proof (Fourier transform duality).* The Fourier transform  $\mathcal{F} : f \mapsto \hat{f}$  is a linear bijection between  $L^1$  and bounded continuous functions, satisfying the Plancherel identity  $\int |f|^2 = (2\pi)^{-d} \int |\hat{f}|^2$  for  $f \in L^2$ . Since  $e^{i\omega^\top x}$  is the kernel of this transform,

$$\begin{aligned} \int f(x) P(dx) &= \int f(x) \left( \frac{1}{(2\pi)^d} \int e^{-i\omega^\top x} \varphi_P(\omega) d\omega \right) dx \\ &= \frac{1}{(2\pi)^d} \int \hat{f}(\omega) \varphi_P(\omega) d\omega. \end{aligned} \quad (22)$$

If  $\varphi_P$  is known everywhere, the right-hand side gives  $\int f dP$  for all  $f \in L^1 \cap L^2$ , implying uniqueness of  $P$ .  $\square$

**Proposition 6** (Lévy’s continuity theorem: weak convergence and uniqueness). *Let  $\{P_n\}$  be a sequence of probability measures on  $\mathbb{R}^d$  with characteristic functions  $\varphi_{P_n}$ . Suppose that  $\varphi_{P_n}(\omega) \rightarrow \varphi(\omega)$  for each  $\omega$ , and that the limit  $\varphi$  is itself a characteristic function (i.e. positive definite and  $\varphi(0) = 1$ ). Then  $P_n \Rightarrow P$ , where  $P$  is the distribution with CF  $\varphi$ . In particular, if  $\varphi_P(\omega) \equiv \varphi_Q(\omega)$  for all  $\omega$ , then  $P = Q$ .*

*Proof (weak convergence via Fourier test functions).* For any  $f \in C_c^\infty(\mathbb{R}^d)$ , its Fourier transform  $\hat{f}$  is rapidly decaying. By Fubini and dominated convergence,

$$\begin{aligned} \int f(x) P_n(dx) &= \frac{1}{(2\pi)^d} \int \hat{f}(\omega) \varphi_{P_n}(\omega) d\omega \xrightarrow{n \rightarrow \infty} \\ \frac{1}{(2\pi)^d} \int \hat{f}(\omega) \varphi(\omega) d\omega &= \int f(x) P(dx). \end{aligned} \quad (23)$$

Hence  $\int f dP_n \rightarrow \int f dP$  for all  $f \in C_c^\infty$ , which implies  $P_n \Rightarrow P$  by the Portmanteau theorem. Taking  $P_n = P$  and  $\varphi_P = \varphi_Q$  gives the uniqueness  $P = Q$ .  $\square$

**Proposition 7** (Bochner’s theorem: positive-definite functions as Fourier transforms of measures). *A continuous function  $\psi : \mathbb{R}^d \rightarrow \mathbb{C}$  with  $\psi(0) = 1$  is the characteristic function of some probability measure on  $\mathbb{R}^d$  if and only if it is positive definite, i.e. for all  $n \in \mathbb{N}$ , all  $\omega_1, \dots, \omega_n \in \mathbb{R}^d$ , and all  $c_1, \dots, c_n \in \mathbb{C}$ ,*

$$\sum_{i,j=1}^n c_i \bar{c}_j \psi(\omega_i - \omega_j) \geq 0.$$

*Moreover, for every finite nonnegative measure  $\mu$  on  $\mathbb{R}^d$ , its Fourier transform  $\psi(\omega) := \int e^{i\omega^\top x} d\mu(x)$  is continuous and positive definite. Thus, continuous positive-definite functions with  $\psi(0) = 1$  are in one-to-one correspondence with characteristic functions of probability measures.*

*Proof (spectral representation).* For any finite positive measure  $\mu$ ,  $\psi(\omega) = \int e^{i\omega^\top x} d\mu(x)$  is continuous and satisfies the positive-definite inequality above by direct calculation. Conversely, if  $\psi$  is continuous and positive definite, by the classical Bochner–Khinchine theorem there exists a unique finite nonnegative measure  $\mu$  such that  $\psi$  is its Fourier transform. Setting  $\mu(\mathbb{R}^d) = 1$  gives a probability measure  $P = \mu$ , with  $\psi = \varphi_P$ .  $\square$

**Proposition 8** (Matching characteristic functions on  $\mathbb{R}^d$  equals to matching the joint distribution). *Let  $P, Q$  be Borel probability measures on  $\mathbb{R}^d$  with characteristic functions  $\varphi_P, \varphi_Q$ . Define a nonnegative weighting function  $w \in L^1(\mathbb{R}^d)$  satisfying  $\text{supp}(w) = \mathbb{R}^d$  and the frequency-domain distance*

$$\mathcal{D}_w^2(P, Q) := \int_{\mathbb{R}^d} w(\omega) |\varphi_P(\omega) - \varphi_Q(\omega)|^2 d\omega.$$

*Then the following are equivalent:*

$$\begin{aligned} \mathcal{D}_w(P, Q) = 0 &\iff \varphi_P(\omega) = \varphi_Q(\omega) \quad \forall \omega \\ &\iff P = Q. \end{aligned} \quad (24)$$

*Proof (Lévy–Bochner synthesis).* If  $\mathcal{D}_w(P, Q) = 0$ , then  $\varphi_P = \varphi_Q$  almost everywhere on  $\{\omega > 0\}$ . Since both  $\varphi_P, \varphi_Q$  are continuous, equality extends to all  $\omega \in \mathbb{R}^d$ . By Proposition 6,  $\varphi_P \equiv \varphi_Q$  implies  $P = Q$ . Conversely, if  $P = Q$ , then clearly  $\mathcal{D}_w(P, Q) = 0$ . Thus, equality of CFs on the full frequency domain is equivalent to equality of the underlying distributions.  $\square$

Intuitively,  $\mathcal{D}_w(P, Q)$  measures the squared discrepancy between characteristic functions across all frequencies, weighted by  $w$ . When  $w$  has full support, this distance captures the complete distributional difference. We now connect this frequency-domain view to kernel methods via Bochner’s theorem.

**Proposition 9** (Kernel formulation via Bochner’s theorem). *Let  $k(x, y) = \kappa(x - y)$  be a bounded, continuous, translation-invariant kernel with spectral measure  $\Lambda$  satisfying*

$$\kappa(t) = \int_{\mathbb{R}^d} e^{i\omega^\top t} d\Lambda(\omega).$$

*Then the maximum mean discrepancy (MMD) between  $P, Q$  in the RKHS of  $k$  admits the spectral representation*

$$\text{MMD}_k^2(P, Q) = \int_{\mathbb{R}^d} |\varphi_P(\omega) - \varphi_Q(\omega)|^2 d\Lambda(\omega).$$

*Moreover, if the kernel is characteristic—equivalently, the support of  $\Lambda$  is all of  $\mathbb{R}^d$ —then  $\text{MMD}_k(P, Q) = 0$  if and only if  $P = Q$ .*

*Proof (spectral integration).* Expanding expectations and applying Bochner’s representation,

$$\begin{aligned} \mathbb{E} k(X, Y) &= \int_{\mathbb{R}^d} \mathbb{E} e^{i\omega^\top (X-Y)} d\Lambda(\omega) \\ &= \int_{\mathbb{R}^d} \varphi_P(\omega) \overline{\varphi_Q(\omega)} d\Lambda(\omega). \end{aligned} \quad (25)$$

Substituting into the definition  $\text{MMD}_k^2(P, Q) = \mathbb{E} k(X, X') + \mathbb{E} k(Y, Y') - 2\mathbb{E} k(X, Y)$  yields the stated formula. If  $\text{MMD}_k(P, Q) = 0$  while  $\Lambda$  has full support, the integrand’s continuity forces  $\varphi_P \equiv \varphi_Q$ , which by Proposition 6 implies  $P = Q$ .  $\square$

**Summary and Connection to CFD.** Propositions 2–6 collectively establish that a probability distribution is uniquely and completely determined by its characteristic function, and that matching characteristic functions over the entire frequency domain—either directly via a weighted  $L^2$  distance  $\mathcal{D}_w$  or indirectly via a characteristic kernel MMD—is equivalent to matching the full joint distribution. The Fourier inversion theorem connects CFs to densities, Bochner’s theorem connects positive-definite kernels

to spectral measures, and Lévy’s continuity theorem ensures that equality of CFs implies equality of distributions. Consequently, frequency-domain metrics such as our CFD provide a principled way to capture all moments and dependencies, beyond what marginal or covariance-based criteria can express.

## H. Moments and Cumulants via Taylor Expansion of Characteristic Functions

### H.1. Preliminaries and Notations

Let  $X = (X_1, \dots, X_d) \in \mathbb{R}^d$  be a random vector with law  $P$ . Its *characteristic function* (CF) is

$$\varphi(\omega) = \mathbb{E}[e^{i\omega^\top X}], \quad \omega = (\omega_1, \dots, \omega_d) \in \mathbb{R}^d,$$

and the *log-characteristic function* (log-CF) is  $\psi(\omega) = \log \varphi(\omega)$  whenever  $\varphi(\omega) \neq 0$ .

**Multi-index notation.** A *multi-index* is  $\alpha = (\alpha_1, \dots, \alpha_d) \in \mathbb{N}_0^d$  with  $|\alpha| := \sum_{j=1}^d \alpha_j$ ,  $\alpha! := \prod_{j=1}^d \alpha_j!$ ,  $\omega^\alpha := \prod_{j=1}^d \omega_j^{\alpha_j}$ , and  $X^\alpha := \prod_{j=1}^d X_j^{\alpha_j}$ . The mixed partial derivative is

$$\partial^\alpha := \frac{\partial^{|\alpha|}}{\partial \omega_1^{\alpha_1} \dots \partial \omega_d^{\alpha_d}}.$$

**Standing condition (finite moment of order  $|\alpha|$ ).** Throughout, whenever we speak of  $\partial^\alpha \varphi(0)$  we assume  $\mathbb{E}|X^\alpha| < \infty$ . This ensures, via dominated convergence, that differentiation and expectation can be interchanged.

### H.2. Limitations of Marginal-Only Matching

Classical matching of *univariate* moments (per-coordinate means/variances/skewness/kurtosis) aligns only the marginals  $\{P_{X_j}\}_{j=1}^d$ . However, cross-variable dependence (pairwise, triple-wise, and beyond) lives in *mixed* moments such as  $\mathbb{E}[X_i X_j]$ ,  $\mathbb{E}[X_i X_j X_k]$ , etc. Hence, marginal-only criteria cannot in general control the joint distribution. We next show that the CF and its derivatives at the origin provide an exact, layered access to all mixed moments/cumulants, thereby capturing dependence.

### H.3. Taylor Coefficients and Mixed Moments/ Cumulants

**Proposition 10** (Derivative–Moment Correspondence). *Suppose  $\mathbb{E}|X^\alpha| < \infty$ . Then*

$$\partial^\alpha \varphi(0) = i^{|\alpha|} \mathbb{E}[X^\alpha]$$

for every multi-index  $\alpha \in \mathbb{N}_0^d$ .

*Proof.* Write  $e^{i\omega^\top X} = \prod_{j=1}^d e^{i\omega_j X_j}$  and differentiate. Each differentiation w.r.t.  $\omega_j$  contributes a factor  $iX_j$ . Thus

$\partial^\alpha e^{i\omega^\top X} = (iX_1)^{\alpha_1} \dots (iX_d)^{\alpha_d} e^{i\omega^\top X}$ . Taking expectation and setting  $\omega = 0$  yields the claim, with the interchange of differentiation and expectation justified by  $\mathbb{E}|X^\alpha| < \infty$ .  $\square$

**Low-order examples.** For  $\alpha = e_j$  (the  $j$ -th unit vector),  $\partial^\alpha \varphi(0) = i \mathbb{E}[X_j]$  (means). For  $\alpha = e_j + e_k$ ,  $\partial^\alpha \varphi(0) = -\mathbb{E}[X_j X_k]$  (mixed second moments). For  $\alpha = e_i + e_j + e_k$ ,  $\partial^\alpha \varphi(0) = -i \mathbb{E}[X_i X_j X_k]$  (triple mixed moments).

**Proposition 11** (Multivariate Taylor expansion of  $\varphi$  at 0). *Under  $\mathbb{E}|X^\alpha| < \infty$  for all  $|\alpha| \leq m$ ,*

$$\begin{aligned} \varphi(\omega) &= \sum_{|\alpha| \leq m} \frac{1}{\alpha!} \partial^\alpha \varphi(0) \omega^\alpha + o(\|\omega\|^m) \\ &= \sum_{|\alpha| \leq m} \frac{i^{|\alpha|}}{\alpha!} \mathbb{E}[X^\alpha] \omega^\alpha + o(\|\omega\|^m). \end{aligned} \quad (26)$$

Define  $\psi(\omega) = \log \varphi(\omega)$  (well-defined near 0 since  $\varphi(0) = 1$  and  $\varphi$  is continuous).

**Definition 1** (Log-Characteristic Function and Mixed Cumulants). *For a multi-index  $\alpha \neq 0$  with  $\mathbb{E}|X^\alpha| < \infty$ , the mixed cumulant is*

$$\kappa_\alpha := i^{-|\alpha|} \partial^\alpha \psi(0)$$

(with  $\kappa_0 := 0$  by convention).

**Proposition 12** (Derivative–Cumulant correspondence). *Assume the moments needed are finite so that  $\psi$  is  $|\alpha|$ -times differentiable at 0. Then the coefficients of the multivariate Taylor series of  $\psi$  at 0 equal the mixed cumulants:*

$$\begin{aligned} \psi(\omega) &= \sum_{|\alpha| \geq 1} \frac{1}{\alpha!} \partial^\alpha \psi(0) \omega^\alpha = \sum_{|\alpha| \geq 1} \frac{i^{|\alpha|}}{\alpha!} \kappa_\alpha \omega^\alpha \\ &\text{(convergent near 0).} \end{aligned} \quad (27)$$

*Proof.* By the chain rule,  $\nabla \psi = \nabla \varphi / \varphi$  and  $\nabla^2 \psi = (\nabla^2 \varphi) / \varphi - (\nabla \varphi \nabla \varphi^\top) / \varphi^2$ , etc. Evaluating at 0 and using Prop. 10:

$$\begin{aligned} \nabla \psi(0) &= i \mathbb{E}[X], \\ \nabla^2 \psi(0) &= -(\mathbb{E}[X X^\top] - \mathbb{E}[X] \mathbb{E}[X]^\top) = -\text{Cov}(X). \end{aligned} \quad (28)$$

Higher-order derivatives of  $\psi$  yield the classical cumulant tensors (via the multivariate Faà di Bruno formula). Collecting terms gives the stated Taylor expansion with coefficients  $\partial^\alpha \psi(0) = i^{|\alpha|} \kappa_\alpha$ .  $\square$

**Interpretation and examples.**  $\kappa_{e_j} = \mathbb{E}[X_j]$  (means);  $\kappa_{e_j+e_k} = \text{Cov}(X_j, X_k)$  (covariance); third-order  $\kappa_{e_i+e_j+e_k}$  measure non-Gaussian triple interactions (synergy/redundancy). In general, *cross-block independence* forces all mixed cumulants spanning the blocks to vanish, making cumulants a clean diagnostic of dependence.

### Implications

- Moments:  $\partial^\alpha \varphi(0) = i^{|\alpha|} \mathbb{E}[X^\alpha]$  reveals *all* mixed moments at each order  $|\alpha|$ .
- Cumulants:  $\partial^\alpha \psi(0) = i^{|\alpha|} \kappa_\alpha$  isolates genuine interactions (they are additive for independent sums and vanish across independent groups).
- Hence, matching  $\varphi$  (or  $\psi$ ) near 0 across *all* multi-indices matches *all* mixed moments/cumulants, aligning dependence at every order.

## I. Additional Analysis on PD-CFD

Using the CUB-200-2011.<sup>1</sup> bird dataset illustrated in Fig. 14, we evaluate how PD-CFD improves the phase-focusing behavior of NCFM.<sup>2</sup> The CUB-200-2011 dataset contains extremely fine-grained categories where discriminative information resides mainly in high-frequency components such as feather textures. Therefore, the loss must be sensitive to detailed structural variations.

We first revisit the original NCFM loss:

$$\begin{aligned} \text{Chf}(t; f) &= \alpha \left( \left| \Phi_{f(x)}(t) - \Phi_{\hat{f}(x)}(t) \right|^2 \right) \\ &+ (1 - \alpha) \left| \Phi_{f(x)}(t) \right| \left| \Phi_{\hat{f}(x)}(t) \right| \left( 1 - \cos \left( a_{f(x)}(t) - a_{\hat{f}(x)}(t) \right) \right) \end{aligned} \quad (29)$$

where  $\Phi$  denotes the characteristic function magnitude and  $a(\cdot)$  the phase.

Although NCFM applies different hyperparameters to amplitude and phase, the phase term is still tightly entangled with amplitude through the multiplicative magnitude factor. As frequency increases, the amplitude decays, causing the phase contribution to be increasingly suppressed. As a result, the mid- and high-frequency phases—even those that still contain meaningful structural information—are overwhelmed and incorrectly treated as noise. To illustrate this behavior, we visualize phase differences across frequencies in Fig. 12: low-frequency phase remains stable, mid-frequency phase begins to drift, and high-frequency phase becomes dominated by boundary noise. However, some med- and med-high-frequency phase components are still reliable and should not be discarded prematurely.

<sup>1</sup>C. Wah, S. Branson, P. Welinder, P. Perona, and S. Belongie, *Caltech-UCSD Birds-200-2011 Dataset*, Technical Report CNS-TR-2011-001, California Institute of Technology, 2011.

<sup>2</sup>Wang et al., *Dataset Distillation with Neural Characteristic Function: A Minimax Perspective*, in *Proc. IEEE/CVF Conf. Comput. Vis. Pattern Recognit. (CVPR)*, 2025, pp. 25570–25580.

To restore these informative phase components, we extend the NCFM loss by adding an explicit phase constraint defined for each sampled frequency  $\omega \sim p(t)$  that is decoupled from amplitude :

$$\begin{aligned} \text{Chf}(t; f) &= \alpha \left( \left| \Phi_{f(x)}(t) - \Phi_{\hat{f}(x)}(t) \right|^2 \right) \\ &+ (1 - \alpha) \left| \Phi_{f(x)}(t) \right| \left| \Phi_{\hat{f}(x)}(t) \right| \left( 1 - \cos \left( a_{f(x)}(t) - a_{\hat{f}(x)}(t) \right) \right) \\ &+ \frac{\lambda_p}{1 + \beta \|\omega\|^2} \left( \theta_{f(x)}(t) - \theta_{\hat{f}(x)}(t) \right)^2, \end{aligned} \quad (30)$$

This additional phase term explicitly extracts the remaining reliable phase information that is otherwise buried by amplitude attenuation in the original NCFM formulation. In particular, it allows mid-frequency phase—which is still semantically meaningful but degraded by the amplitude coupling—to be effectively preserved.

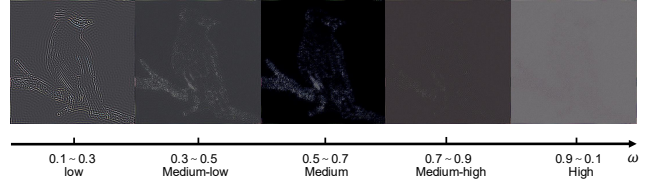


Figure 12. Phase information under different frequency band



Figure 13. Comparison between generated data with original loss function and PD-CFD loss.

We verify the effect of this decoupled phase constraint under downstream classification accuracy and results are illustrated in Table. 10 (see Fig. 13 for an example of the synthetic image). The results match our expectation: when  $\lambda_p = 0.3$ , the added phase regularization significantly strengthens high-frequency alignment, especially for the feather and edge regions in the CUB images.

Table 10. Effect of phase regularization  $\lambda_p$  on accuracy.

| $\lambda_p$ | Accuracy (%) | Improvement |
|-------------|--------------|-------------|
| 0.0         | 23.80        | 0           |
| 0.1         | 24.15        | 1.47%       |
| 0.2         | 25.20        | 5.88%       |
| 0.3         | 28.35        | 19.12%      |

A similar phenomenon is observed on the DTD and RESISC-45 datasets (illustrated in Fig. 15 Fig. 16 respec-

tively). The DTD texture dataset contains a large amount of rapidly oscillating material patterns characterized by abrupt edge transitions, fine-scale boundaries, and dense local contour variations. Likewise, the RESISC-45 remote-sensing dataset exhibits substantial geometric complexity: land-cover boundaries, building edges, road networks, rooftop outlines, and other high-frequency landscape structures that vary sharply across classes. These discriminative details are dominated by high-order moment information in the frequency domain. Traditional metrics such as MSE or CE are inherently insensitive to such structural discontinuities—they primarily respond to low-order statistics and smooth variations, and therefore fail to capture the fine-grained distributional differences arising from high-frequency contours and edge transitions.

In contrast, our PD-CFD formulation introduced earlier can naturally recover these informative distributional discrepancies. By removing the amplitude-induced suppression of mid- and high-frequency phase, PD-CFD preserves the remaining reliable phase components that encode exactly these texture- and edge-based variations. Consequently, FAST maintains strong performance even on challenging datasets such as DTD and RESISC-45, where structural information is dominated by, high-frequency features and where competing baselines degrade substantially.



Figure 14. CUB-200-2011 Bird Dataset

## J. Experiments on Language Tasks

### J.1. Setup

To further evaluate the generalization capability of FAST on LLM datasets, we conduct experiments on the Alpaca instruction-following dataset. Following our main setup, we adopt LLaMA2-7B as the backbone and apply LoRA-based fine-tuning using core-sets sampled at retention rates of 10%, 20%, and 30%. For evaluation, we report performance on the MMLU benchmark, which spans 57 diverse subjects and serves as a rigorous protocol for assessing broad knowledge and reasoning abilities. We compare FAST against the NMS baseline<sup>3</sup>, the current SOTA method, under identical experimental settings.

### J.2. Results

The MMLU results are shown in Fig. 17. Across all keep ratios, FAST consistently outperforms the NMS baseline. While NMS attains an average accuracy of approximately 33%, FAST increases the performance to 39%, corresponding to a relative improvement of about 18%. These results indicate that FAST is highly effective at selecting and preserving semantically informative instances. Moreover, the strong performance gains suggest that high-level semantic structure can be retained through spectral-graph-based distribution alignment alone, without explicit reliance on neural feature extractors. By leveraging geometric and frequency-domain signals, FAST preserves the underlying semantic neighborhood relations required for downstream reasoning. This demonstrates the robustness and broad generalization ability of FAST, even on tasks that rely heavily on semantic consistency.

<sup>3</sup>Boran Zhao et al., *NMS: Efficient Edge DNN Training via Near-Memory Sampling on Manifolds*, arXiv preprint arXiv:2508.02313, 2025.

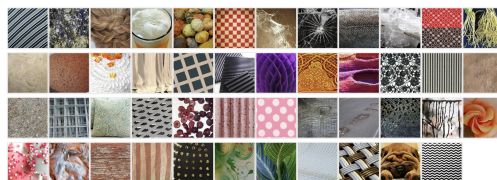


Figure 15. DTD Texture Dataset

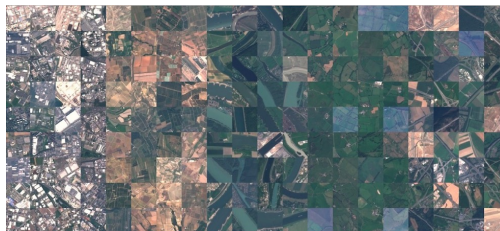
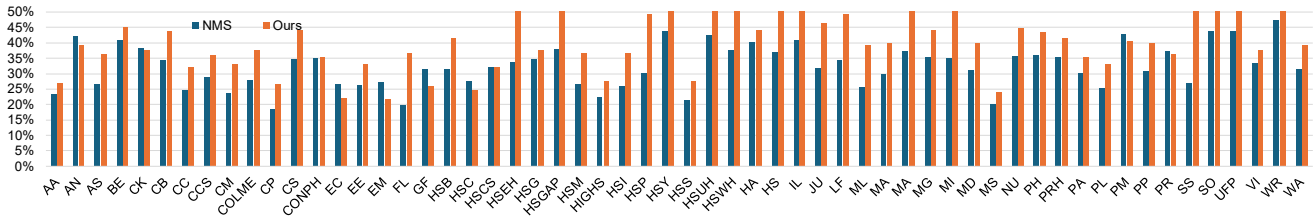
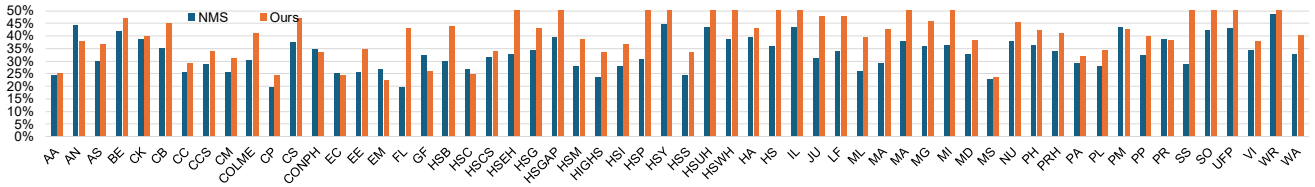


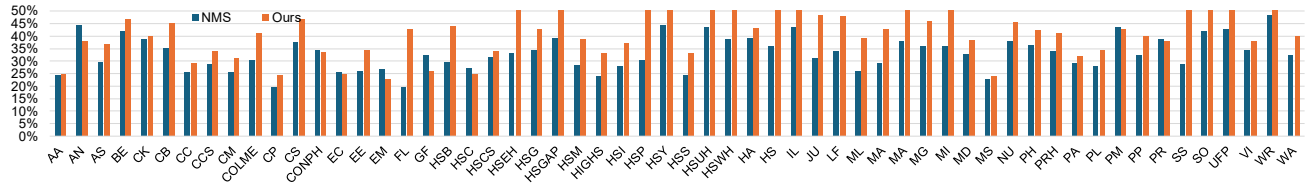
Figure 16. RESISC-45 Remote Sensing Dataset



(a) Keep ratio 10%



(b) Keep ratio 20%



(c) Keep ratio 30%

Figure 17. MMLU accuracy comparison at different keep ratios.